Consistent determination of the heating rate of light-absorbing aerosol using wavelength- and time-dependent Aethalometer multiple-scattering correction

L. Ferrero[1], V. Bernardoni[2], L. Santagostini[1], S. Cogliati[1,3], F. Soldan[2], S. Valentini[2], D. Massabò[4], G. Močnik[5,6], A. Gregorič[5,7], M. Rigler[7], P. Prati[4], A. Bigogno[1], N. Losi[1], G. Valli[2], R. Vecchi[2], E. Bolzacchini[1]

[1]GEMMA and POLARIS Centre, Università degli Studi di Milano-Bicocca, 20126 Milano, Italy

[2]Dipartimento di Fisica "A. Pontremoli", Università degli Studi di Milano & INFN-Milan, 20133 Milano, Italy

[3]Remote Sensing of Environmental Dynamics Lab., DISAT, University of Milano-Bicocca, P.zza della Scienza 1, 20126, Milano, Italy

[4]Dip. di Fisica Università di Genova & INFN Sezione di Genova, Via Dodecaneso 33, 16146 Genova, Italy

[5]Center for Atmospheric Research, University of Nova Gorica, SI-5000 Nova Gorica, Slovenia

[6]Department of Condensed Matter Physics, Jozef Stefan Institute, Jamova 39, SI-1000 Ljubljana, Slovenia

[7] Aerosol d.o.o., Kamniška 39A, SI-1000 Ljubljana, Slovenia

Correspondence to: Luca Ferrero (luca.ferrero@unimib.it)

Abstract. Accurate and temporally consistent measurements of light absorbing aerosol (LAA) heating rate (HR) and of its source apportionment (fossil-fuel, FF; biomass-burning, BB) and speciation (black and brown Carbon; BC, BrC) are needed to evaluate LAA short-term climate forcing. For this purpose, wavelength- and time-dependent accurate LAA absorption coefficients are required. HR was experimentally determined and apportioned (sources/species) in the EMEP/ACTRIS/COLOSSAL-2018 winter campaign in Milan (urban-background site). Two Aethalometers (AE31/AE33) were installed together with a MAAP, CPC, OPC, a low volume sampler ($PM_{2.5}$) and radiation instruments. AE31/AE33 multiple-scattering correction factors (C) were determined using two reference systems for the absorption coefficient: 1) 5-wavelength PP_UniMI with low time resolution (12 h, applied to $PM_{2.5}$ samples); 2) timely-resolved MAAP data at a single wavelength. Using wavelength- and time-independent *C* values for the AE31 and AE33 obtained with the same reference device, the total HR showed a consistency (i.e. reproducibility) with average values comparable at 95% probability. However, if different reference devices/approaches are used, i.e. MAAP is chosen as reference instead of a PP_UniMI, the HR can be overestimated by 23-30% factor (by both AE31/AE33). This became more evident focusing on HR apportionment: AE33 data (corrected by a wavelength- and time-independent C) showed higher HR_{FF} (+24±1%) and higher HR_{BC} (+10±1%) than that of AE31. Conversely, HR_{BB} and HR_{BrC} were -28±1% and -29±1% lower for AE33 compared to AE31. These inconsistencies were overcome by introducing a wavelength-dependent C_λ for both AE31 and AE33, or using multi-wavelength apportionment methods, highlighting the need for further studies on the influence of wavelength corrections for HR determination. Finally, the temporally-resolved determination of *C* resulted in a diurnal cycle of the HR not statistically different whatever the source- speciation- apportionment used.

KEYWORDS: Heating rate; Black Carbon; Brown Carbon; Fossil Fuel; Biomass Burning; COLOSSAL.

1. Introduction

Light absorbing aerosols (LAA: e.g. black carbon, BC; brown carbon, BrC; and dust) are important due to their optical and radiative forcing properties (Laskin et al., 2015; Petzold et al., 2013; Bond et al., 2013). Accordingly to IPCC (2013) and several authors (Bond et al., 2013; Ramanathan and Carmichael, 2008), the BC is the second most important positive anthropogenic climate-forcing agent after CO_2 (top-of-atmosphere direct forcing of ~0.71 W m^{-2}; range 0.08 - 1.27 W m^{-2}). In addition to BC, BrC may contribute ~10-30% to the total solar absorption induced by LAA (Chung et al., 2012; Shamjad et al., 2015; Laskin et al., 2015; Ferrero et al., 2018). Finally, dust aerosol could promote an atmospheric forcing in the range -0.1±0.2 W m^{-2} (Myhre et al., 2013), rising up regionally to ~80-100 W m^{-2} (Huang et al., 2009; Mallet et al., 2009). Unlike CO_2, which is distributed quite homogeneously in the atmosphere, LAA are short-lived climate forcers (~1 to several weeks of residence time) (Samset et al., 2013; Cape et al., 2012); thus, their effect could be counteracted by short-term climate strategies (Ødemark et al., 2012; Shindell et al., 2012; Jacobson, 2010; Quinn et al., 2008). This would lead enough time to CO_2 related sustainability strategies and renewable energy to become fruitful (Qerimi et al., 2020; Kibaara et al., 2020; Burciaga, 2020) to avoid the dramatic environmental effects of climate change (e.g. Javadinejad et al., 2020; Oo et al., 2020). However, to adopt the right mitigation strategies on LAA, the identification of the relative importance of different sources and species of LAA on the total HR is required with a clear need to reduce the uncertainties related to their determination (Ferrero et al., 2018; Myhre et al., 2013) as well as to properly quantify their atmospheric feedbacks (Su et al., 2020; Tian et al., 2019; Diemoz et al, 2019; Ferrero et al., 2011a, 2014, 2016, 2019a,b; Ran et al., 2016; Costabile et al., 2013; Lemaître et al., 2010). For example, LAA can affect: the atmospheric stability (Su et al., 2020), the pattern of synoptic winds such as the monsoon (Bond et al., 2013; Ramanathan and Feng, 2009; Koch et al., 2009; Ramanathan and Carmichael, 2008; Koren et al. 2008; Koren et al., 2004; Kaufman et al., 2002), the cloud distribution (Matus et al., 2015; Koch and Del Genio, 2010) thus modulating the amount and the spectrum of the short-wave radiation that reaches the ground (Ferrero et al., 2021; Črnivec and Mayer, 2019). Finally, the high UV-VIS absorption of BrC can influence the photolysis rate in the atmosphere affecting the concentration of other atmospheric pollutants, such as the ozone (Laskin et al., 2015 and references therein). Thus, in order to deal with the aforementioned feedbacks, a proper determination of the HR induced by LAA is required.

To achieve this goal, accurate measurements of the wavelength-dependent absorption coefficient ($b_{abs}(\lambda)$) in the UV-VIS-IR region are required. In fact, when the HR is directly experimentally determined (Ferrero et al., 2018, 2021), or when radiative transfer models are used to compute the HR (Tian et al., 2019; Gao et al., 2008), $b_{abs}(\lambda)$ is integrated over the whole shortwave spectrum (in synergy with the radiation; see section 2.1); thus, even a small bias on any $b_{abs}(\lambda)$ can be magnified by the integral operation.

For measuring the LAA $b_{abs}(\lambda)$ in the whole UV-VIS-NIR region, Aethalometers (e.g. AE31 and AE33) are the most common and widely used devices. They feature a wide range of spectral channels (7-λ: 370, 470, 520, 590, 660, 880 and 950 nm) not available in other instruments (e.g. MAAP, PSAP, photoacoustic spectrometer) (Petzold et al., 2005; Virkkula et al., 2010; Arnott et al., 1999). This spectral range is needed for the experimental HR determination (and radiative transfer models) as it includes the portion of the solar spectrum mainly responsible for incoming energy (Ferrero et al., 2018). Moreover, Aethalometers take also the advantage of global long-term data series (Ferrero et al., 2016; Eleftheriadis et al., 2009; Collaud-Coen et al., 2010; Junker et al., 2006) that could be used in the near future to retrieve historical series of the HR.

Despite the aforementioned advantages, the disadvantage (common to any filter-based absorption technique) is the need to compensate for three kinds of artefacts (Liousse et al., 1993; Petzold et al., 1997; Bond et al., 1999): 1) the multiple scattering (enhanced light attenuation and optical path by multiple scattering by the filter fibres); 2) the aerosol backscattering (light attenuation is further enhanced due to scattering of aerosols embedded in the filter); 3) the loading effect (the non-linear optical path reduction induced by absorbing particles accumulating in the filter). To account for the loading effects, Aethalometers data are traditionally corrected applying the procedures reported in Weingartner et al. (2003) and Collaud-Coen et al. (2010) for AE31 or in Drinovec et al. (2015) for AE33. All these procedures, require an accurate determination of the filter multiple scattering correction parameter *C* (Schmid et al., 2006; Arnott et al., 2005, Weingartner et al., 2003). Several estimates of *C* values are reported in the literature, ranging from 2.14 up to 5 (Weingartner et al., 2003; Arnott et al., 2005; Schmid et al., 2006; Sandradewi et al., 2008a, 2008b; Collaud Coen et al., 2010; GAW, 2016). As recently demonstrated, *C* values can vary with the Aethalometer type, Aethalometer filter material, time (diurnal/seasonal pattern) and wavelength (Bernardoni et al., 2021; Yus-Díez et al., 2021). Any arbitrary assumption on the C values (avoiding to control the influence of the aforementioned parameters) will influence the determination of the LAA optical properties and their apportionment in terms of source and species (Sandradewi et al., 2008a; Massabò et al., 2015; Bernardoni et al., 2017; Tian et al., 2019); this will reflect on the HR source-species quantification too. Thus, accurate measurements of the wavelength-dependent absorption coefficient ($b_{abs}(\lambda)$) in the UV-VIS-IR region are required.

Moreover, Andreae and Ramanathan (2013) report that radiative model results can be characterized by large discrepancies among each other, amplifying the uncertainties related to implications for the global and regional climate; among the whole ensemble of uncertainties, LAA optical properties play a major role (Nordmann et al., 2014; Koch et al., 2009). As a conclusion, Andreae and Ramanathan (2013) declared the need for better observational constraints at all scales, while Chung et al. (2012) and Samset at al. (2018) called for model independent, observationally based estimate of the LAA properties.

Recently, Ferrero et al. (2018, 2021) developed a novel methodology to experimentally quantify the HR induced by LAA. This method enables to provide experimental LAA-HR data at high-time resolution with an accessible technique applicable in any established aerosol monitoring network (e.g. EMEP). The method also allows a source-related (i.e. fossil-fuel, FF; biomass-burning, BB) or a species-related (e.g. BC, BrC) apportionment of the HR.

Thus, the current paper applies the aforementioned experimental method for HR determination in function of different wavelength and temporal parametrizations of the multiple scattering parameter C with the aims to:

- quantify the C influence on the assessment of the experimental total, source (FF, BB), and species (BC, BrC) HR;

- determine the best practice procedures for Aethalometer multiple-scattering correction for radiative forcing assessment purposes.

A special attention is given both to the temporal consistency – important in any measurement time series where AE31 Aethalometers are supplanted by the newest AE33 version – and to the accuracy of source/species apportionment. The obtained results were determined within the framework of the winter

2018 European EMEP/ACTRIS/COLOSSAL (COST Action CA16109; Chemical On-Line cOmpoSition and Source Apportionment of fine aerosol) WG3 campaign.

The manuscript is organized as follows: in section 2 we will describe the experimental methodology to determine the LAA HR (section 2.1) and the experimental set-up used for determining both the HR and the multiple scattering parameter C (sections 2.2 and 2.3); results and discussion will follow in section 3, describing first the environmental context of atmospheric pollution during the campaign (section 3.1) and then (sections 3.2, 3.3 and 3.4) the HR values (total and from different species and sources of LAA) as a function of different *C* parametrizations. Conclusions follows with a best practice procedure for Aethalometer correction for radiative forcing assessment purposes.

2. Methodology

The LAA heating rate measurements were performed in the city of Milan from 18 January 2018 to 15 February 2018. Milan is situated in the Po Valley which is a European air pollution hotspot, especially during wintertime, when stable atmospheric conditions occur, promoting the accumulation of aerosol within the mixing layer (Crova et al., 2021; Diémoz et al., 2019; Ferrero et al., 2011b, 2012; Vecchi et al., 2004, 2019) which is well visible even from satellites (Ferrero et al., 2019a; Di Nicolantonio et al., 2007, 2009; Barnaba and Gobbi 2004).

The sampling site is located on the rooftop (10 m a.g.l.) of the U9-bulding of the University of Milano-Bicocca (45°30'38" N, 127 9°12'42" E, Italy). The site is characterized by a full hemispherical sky view; moreover, its roof is characterized by a Lambertian concrete surface: due to its flat and homogeneous characteristics, it well represents the average spectral reflectance of the Milano urban area (Ferrero et al, 2018). The U9 is equipped with instrumentation for the measurement of the absorption coefficient and radiation needed to determine the HR (section 2.2) but before introducing them, the HR determination method is detailed in the next section (2.1).

2.1 Heating Rate determination

The HR (K day^{-1}) induced by LAA is determined using the experimental methodology reported in Ferrero et al. (2018, 2020). Here we briefly summarize the method and the reader is referred to the aforementioned publications for the physical demonstration of the approach.

The instantaneous aerosol total HR is determined by combining the LAA multi-wavelength absorption coefficient ($b_{abs}(\lambda)$) and radiation measurements (direct, diffuse or reflected) integrating them over the whole ensemble of shortwave wavelengths and incident angles within the 2π hemisphere from sky and those reflected from the ground as follows:

$$HR = \frac{1}{\rho C_p} \cdot \sum_{n=1}^{3} \int_{\theta} \int_{\lambda} \frac{F_n(\lambda,\theta)}{\cos\theta} b_{abs}(\lambda) d\lambda d\theta \quad (1)$$

where ρ represents the air density (kg m^{-3}), Cp (1005 J kg^{-1} K^{-1}) is the isobaric specific heat of dry air, n is the index indicating the n^{th} type of radiation (n stands for direct, diffuse or reflected) impinging the absorbing aerosol, λ and θ represent the wavelength and zenith angle of the radiation, $F_{n(\lambda,\theta)}$ is the n^{th} type (direct or diffuse or reflected) of monochromatic irradiance of wavelength λ that strikes with an angle θ the aerosol layer.

Under the isotropic (for diffuse radiation from sky and clouds) and Lambertian (for land) assumptions (as used in Ferrero et al., 2018) equation 1 can be solved (see Ferrero et al., 2021) becoming:

$$HR = \frac{1}{\rho C_p} \cdot \left[\frac{1}{cos(\theta_z)} \int_{\lambda} F_{dir}(\lambda)\, b_{abs}(\lambda)\, d\lambda + 2 \int_{\lambda} F_{dif}(\lambda)\, b_{abs}(\lambda)\, d\lambda + 2 \int_{\lambda} F_{ref}(\lambda)\, b_{abs}(\lambda)\, d\lambda \right] \quad (2)$$

where θ_z refers to the solar zenith angle, while $F_{dir}(\lambda)$, $F_{dif}(\lambda)$ and $F_{ref}(\lambda)$ are the spectral direct, diffuse and reflected irradiances.

As already pointed out in Ferrero et al. (2018), it is worth recalling that in the present method (equations 1-2), the HR is independent from the thickness of the investigated atmospheric aerosol layer and thus referred to the altitude at which it is determined. In the present work they were applied to the near-surface atmospheric layer. BC and HR vertical profiles data previously collected at the same site revealed that they were constant inside the mixing layer (Ferrero et al., 2014). Despite this limit, the HR measurement has significant advantages: 1) no radiative transfer assumptions are needed (i.e. clear sky situation), 2) measurements are carried out at high time resolution allowing to follow the HR dynamic, 3) measurements are carried out in any sky conditions allowing to manage a continuous time series.

In addition to these advantages, the method allows a source-related (i.e. fossil-fuel, biomass-burning) or a species-related (e.g. BC, BrC) apportionment of the HR. In fact, the spectral dependence of the aerosol absorption coefficient ($b_{abs}(\lambda)$) is generally described by the power-law relationship $b_{abs} \propto \lambda^{-AAE}$ where AEE is the Ångström absorption exponent (Moosmüller et al., 2009, 2011). The AAE is a parameter useful for the apportionment of carbonaceous aerosol into different species (BC and BrC) and sources (FF and BB) (Tian et al., 2019; Massabò et al., 2015, Sandradewi et al., 2008a). Thus, any $b_{abs}(\lambda)$ apportionment method also allows to apportion the contribution to the HR of the different LAA species (HR_{BC} and HR_{BrC}) and sources (HR_{FF} and HR_{BB}) by applying eq. 1-2. Source specific AAE values (AAE_{FF} and AAE_{BB}) in Milan were set as 1 and 2 on the basis of previous investigations in the same area (Bernardoni et al., 2017, 2021). BrC is characterized by AAE_{BrC} values which can vary in literature from 3 to 10 (Ferrero et al., 2018; Shamjad et al., 2015, Massabò et al., 2015; Srinivas et al., 2013; Yang et al., 2009; Kirchstetter et al., 2004).

From a general point of view, any traditional apportionment of the species and sources is based on four equations:

$$\frac{b_{abs}(\lambda_1)_A}{b_{abs}(\lambda_2)_A} = \left(\frac{\lambda_1}{\lambda_2}\right)^{-\mathrm{AAE_A}} \tag{3}$$

$$\frac{\mathrm{b_{abs}}(\lambda_1)_\mathrm{B}}{\mathrm{b_{abs}}(\lambda_2)_\mathrm{B}} = \left(\frac{\lambda_1}{\lambda_2}\right)^{-\mathrm{AAE_B}} \tag{4}$$

$$\mathrm{b_{abs}}(\lambda_{1,2}) = \mathrm{b_{abs}}(\lambda_{1,2})_\mathrm{A} + \mathrm{b_{abs}}(\lambda_{1,2})_\mathrm{B} \tag{5,6}$$

where A and B two different LAA species (BC, BrC) or sources (FF, BB), λ_1 and λ_2 are two different wavelengths. If AAE_A and AAE_B are chosen a-priori as well as λ_1 and λ_2, we are in the case of the so-called Aethalometer model for FF and BB apportionment (Sandradewi et al., 2008a): in this paper AAE_{FF}=1, AAE_{BB}=2, λ_1=470 nm, λ_2=950 nm. If AAE_A is chosen a-priori and only λ_2 is used, as in Tian et al., (2019), the method allows a BC/BrC apportionment, based on the calculation of $b_{abs}(\lambda)_{\_BC}$ assuming that $b_{abs(950)\_BrC}$=0 at high wavelengths and AAE_{BC}=1; $b_{abs(\lambda)\_BrC}$ is obtained as difference from the total and AAE_{BrC} is estimated on its basis.

If finally, λ_1 and λ_2 are not chosen a-priori, but all possible Aethalometer wavelengths are used, two methods can be applied by fitting $b_{abs}(\lambda)$ over the whole spectrum:

1) the Multi-λ fit approach reported in Bernardoni et al., 2021 from which it follows that

$$b_{abs}(\lambda) = A' \cdot \lambda^{-AAE_{FF}} + B' \cdot \lambda^{-AAE_{BB}} \quad (7)$$

where A' and B' in equation (7) are obtained by multi-λ fit of the input data, assuming a-priori AAE_{FF} and AAE_{BB} values (1 and 2).

2) the MWAA (Multi-Wavelength Absorption Analyzer) model described in previous works (Massabò et al., 2015; Bernardoni et al., 2017) enables to assess the contributions of BC and BrC and to provide information on the AAE_{BrC} by

$$b_{abs}(\lambda) = A'' \cdot \lambda^{-AAE_{BC}} + B'' \cdot \lambda^{-AAE_{BrC}} \quad (8)$$

where A", B" and AAE_{BrC} are obtained by multi-λ fit of the input data, provided that a value for AAE_{BC} is assumed a-priori. It is noteworthy that in the multi-λ fit for the aethalometer model source apportionment (eq. 7), AAE for both sources (AAE_{FF} and AAE_{BB}) must be assumed a priori. Opposite, the MWAA model for LAA species apportionment also provides as output the information on AAE for one of the species (AAE_{BrC}). In this case, AAE_{BC}=AAE_{FF}=1 was chosen as done in previous applications (Bernardoni et al., 2017, Massabò et al., 2015).

Given all the aforementioned methodologies it is clear that the total HR accuracy (eq. 1-2), and thus its apportionment ($HR=HR_{BC}+HR_{BrC}$ or $HR=HR_{FF}+HR_{BB}$), is strictly dependent on the reliability of $b_{abs}(\lambda)$. Thus sections 2.2 and 2.3 are dedicated to the HR instrumentation, Aethalometer correction schemes and the determination of the multiple scattering correction parameter *C*, respectively. The flow chart of the methodological investigation is finally resumed in Figure 1 to improve the readability of the present work.

2.2 HR instrumentation

The methodology for the determination of HR (section 2.1) requires the measurements of $b_{abs}(\lambda)$ in the UV-VIS-NIR region at high time resolution. Therefore, as explained in the introduction (section 1), the only instrument able to fully cover this range is the Aethalometer that performs measurements at 7 wavelengths (370, 470, 520, 590, 660, 880 and 950 nm). During the COLOSSAL campaign two models of Aethalometers (AE) were used in parallel, the AE31 and AE33 (Magee Scientific, Aerosol) with two different filter tapes: a quartz-fibre filter (Pallflex Q250F) for the model AE31, and a tetrafluoroethylene (TFE)-coated glass filter (Pallflex "Fiberfilm" T60A20) for the model AE33 (Drinovec et al., 2015). AE31 and AE33 provide as output equivalent BC (eBC) (Petzold et al., 2013) concentration, and the corresponding optical parameters, at 5- and 1-minute time resolution, respectively.

The AE measure the ATN of light at 7 wavelengths transmitted through a particle laden filter spot and through a sample free portion of the tape acting as a reference. ATN is calculated as:

$$ATN = \ln(I_0/I) \tag{9}$$

where I_0 and I are the intensity of light transmitted through the reference and aerosol blank spot of the filter, respectively. In the Aethalometer the aerosol sample is continuously deposited on one/two spots (AE31/AE33) of a filter tape which moves once an attenuation (ATN) threshold (120) is reached at 370 nm.

The attenuation coefficient of the aerosol particles collected on the filter tape, $b_{ATN(\lambda)}$, is then defined as follows (Weingartner, et al., 2003):

$$b_{ATN(\lambda)} = \frac{A}{Q}\frac{\Delta ATN(\lambda)}{\Delta t} \tag{10}$$

where A is the filter spot area, Q the volumetric low rate and ΔATN is the change in attenuation during the time interval Δt.

It is noteworthy that b_{ATN} differs from the aerosol absorption coefficient of airborne particles because it is determined from attenuation of light passing through a particle-laden filter; the resulting artifacts can be corrected with different procedures (Weingartner, et al. 2003, Arnott, et al., 2005, Schmid, et al. 2006, Collaud Coen, et al. 2010; Drinovec et al., 2015) in function of the Aethalometer model and filter types (section 1).

Aethalometer AE31 artifacts were corrected applying the Weingartner et al. (2003) procedure that introduces the parameters *C* and *R(ATN,λ)*, used to convert $b_{ATN}(\lambda)$ to $b_{abs}(\lambda)$ as follows:

$$b_{abs(\lambda)} = \frac{b_{ATN(\lambda)}}{C \cdot R(ATN,\lambda)} \quad (11)$$

where *C* and *R(ATN,λ)* are the filter multiple scattering correction parameter and the λ-dependent loading effect correction parameter, respectively. The parameter *R(ATN,λ)* compensates for the loading effect due to the reduction in the optical path due to an increase of the sample collected on the filter over time (Weingartner et al., 2003).

R(ATN,λ) was dynamically determined following the Sandradewi et al. (2008b) algorithm. This approach was recognised to be one of the best approaches as correction does not affect data in terms of the absorption Ångström exponent (AAE) (Collaud Coen et al., 2010) and it was previously applied to data collected at the investigated site since 2015 (Ferrero et al., 2018): for the experimental assessment of HR any artificial perturbation of the AAE must be avoided.

The parameter *C* compensates for the enhanced optical path through the filter caused by multiple scattering of the light induced by the filter fibers and by the particles embedded in it. Its determination, in function of time and wavelength, using reference absorption instruments (and application to HR) is discussed in the next section (2.2). Here we recall (see also section 1) that several *C* values are reported in literature, ranging from 2.14 up to 5 (Weingartner et al., 2003; Arnott et al., 2005; Schmid et al., 2006; Sandradewi et al., 2008a, 2008a; Collaud Coen et al., 2010) with a suggested C=3.5 from GAW (2016) constant for all wavelengths of AE31.

In the Aethalometer AE33, the loading artifact is measured and corrected internally due to the DualSpot technology as reported in Drinovec et al. (2015). Thus, in the AE33, $b_{abs}(\lambda)$ is retrieved as follows:

$$b_{abs(\lambda)} = \frac{b_{ATN\_LC(\lambda)}}{C} \quad (12)$$

where $b_{ATN\_LC(\lambda)}$ is the attenuation coefficient already corrected for the loading effect (Drinovec et al., 2015), and *C* is set at 1.57 for tetrafluoroethylene (TFE)-coated glass filter (Pallflex "Fiberfilm" T60A20). The mass absorption cross-section at 880 nm is assumed to be 7.77 $m^2 g^{-1}$.

As the main aim of the present work is the determination of the influence of *C* on the HR for both AE31 and AE33, the methodology to investigate this topic is discussed in the next section (2.3). Here below, other needed measurements for HR determination are described.

In order to determine the HR, irradiance measurements were obtained with a Multiplexer-Radiometer-Irradiometer (MRI) and a meteorological station (LSI-Lastem) equipped with broadband radiometers.

The MRI detects downward and upward irradiance in the UV, visible and in the near-infrared spectrum (UVNIR), from 350 to 1000 nm in 3648 spectral bands. The instrument uses an optical switch to sequentially select among many different fiber optical inputs fixed to the up-looking and the down-looking entrance foreoptics. The fiber optic multiplexer MPM-2000-2x8-VIS (Ocean Optics Inc., USA) is used as an optical switch, connecting up to 8 different input channels into two different spectrometers. In addition, a rotating shadow-band is implemented to allow measurements of direct, diffuse, and reflected irradiance. Further details of the MRI are reported in Cogliati et al. (2015).

The LSI-Lastem meteorological station is equipped with a global pyranometer (DPA154 model) for measuring global irradiance and a net radiometer (C201R model) for net radiation measurements. The combination of a shadow band with another DPA154 pyranometer allows the measurement of diffuse irradiance (either from sky and clouds) and the retrieval of direct irradiance after subtraction from the global one. Before the subtraction the shadow band effect must be corrected (Ferrero et al., 2018) to determine the true amount of diffuse irradiance.

The LSI-Lastem is also equipped with temperature (DMA580 sensor with data range from -30 to +70 °C with an accuracy of ± 0.1 °C and with a sensitivity of 0.025°C), humidity (DMA570 sensor with data range includes values from 10% to 98% with an accuracy of ± 2.5% and sensibility of 0.2%), pressure

(CX110P barometer with data range from 800hPa to 1100 hPa with an accuracy of 1 hPa) and wind (speed and direction, CombiSD anemometer with data range from 0 to 60 m/s and from 0 to 360°) sensors. Finally, the U9 sampling site is equipped with a Condensation Particle Counter (CPC, 3775 TSI) which provides particle number concentration (N; d_{50}=4 nm) in a concentration range from 0 to 10^7 particles/cm^3; in addition, an optical particle counter (OPC, Grimm 1.107) which measured the particle number concentration and size distribution in the range 0.25 - 32 µm and estimated PM_{10}, $PM_{2.5}$ and PM_1 mass concentrations.

2.3 Determination of the multiple-scattering correction parameter *C*

The multiple scattering correction *C* is determined by comparing the attenuation coefficient, already corrected for the loading effect ($b_{ATN\_LC}(\lambda)$; either from AE31 and AE33), with the absorption coefficient measured simultaneously at the same wavelength with a reference instruments ($b_{abs\_ref}(\lambda)$) as follows:

$$C(\lambda) = \frac{b_{ATN\_LC(\lambda)}}{b_{abs\_ref(\lambda)}} \tag{13}$$

Recalling equations 1-2, the HR is directly proportional to the integral (over the whole shortwave spectrum) of the product of $b_{abs}(\lambda)$ and the radiation $F_n(\lambda,\theta)$. Thus, any inappropriate assumption on the *C* value, e.g. it does not vary over wavelengths and time, will impact the HR and its apportionment to sources (FF, BB) and species (BC, BrC). The experimental determination of these impacts and best practice for climate data harmonization is the aim of the present work.

For this reason, two reference instruments for $b_{abs\_ref}(\lambda)$ were used in order to give complementary information:

1- Highly time-resolved measurements at a single, fixed wavelength, using a Multi-Angle Absorption Photometer (MAAP, Thermo Scientific Model 5012)
2- Wavelength-resolved measurements with low time resolution (12 h), using the polar photometer (PP_UniMI, set up at the Department of Physics, University of Milan)

Here below, the two reference instruments are briefly described.

The first reference, the Multi-Angle Absorption Photometer (MAAP, Thermo Scientific Model 5012) measures the aerosol absorption coefficient at a wavelength of 637 nm (Müller et al., 2011) and provides the atmospheric eBC at high time resolution (5 minutes). It simultaneously measures the transmission and scattering of light in the forward and back hemisphere (at 3 different angles) of a blank and a particle laden filter tape. The absorption coefficient at 637 nm is thereafter obtained from a radiative transfer scheme (Petzold and Schönlinner, 2004; Petzold et al., 2005). The eBC is obtained from absorption coefficient considering the deposit area and sampling air flow and setting at 6.6 m^2 g^{-1} the eBC mass-specific absorption coefficient. Compared to AE, instrumental artifacts are reduced in the MAAP so that the absorption coefficient measured should be closer to the true one and therefore it is traditionally used as a reference among filter-based instruments in literature works (Collaud-Coen et al. 2010). With respect to C determination with AE-MAAP comparison we underlined that the nominal AE31 and AE33 660 nm channel is provided by a Kingbright led (APT 1608SRC PRV 1.6 x 0.8 mm SMD Chip LED Lamp; https://www.kingbrightusa.com/images/catalog/SPEC/APT1608SRCPRV.pdf) which is characterized by a wavelength peak emission at 655 nm with a 20 nm spectral full bandwidth at half maximum under 20mA of supplied current (information from manufacturer). This is in agreement with the absorption photometers intercomparison reported by Muller et al. (2011) in which the nominal AE red channel was determined to be at 654 nm with a 23 nm spectral full bandwidth at half maximum; they also reported the same data for the red MAAP channel which is characterized by a wavelength peak emission at 637 nm with an 18 nm spectral full bandwidth at half maximum. Thus, for practical purpose the AE and MAAP work in the red channel approximately at the same wavelength allowing their direct comparison for C determination avoiding to introduce computation noise by reporting the nominal 660 nm channel to 637 nm in function of a delicate AAE determination as demonstrated in the results and discussion sections.

The second reference is the polar photometer (PP_UniMI, set up at the Department of Physics, University of Milan) where different laser sources are mounted on a sliding motor (at the time of this work, 4 laser sources at 405, 532, 635 and 780 nm were used). The chosen laser beam impinges perpendicularly on the aerosol sample and a photodetector is mounted on a rotating arm; it performs measurements of the transmitted and of the scattered radiation at scattering angles between 0° and 173° (with 0.4° resolution). This allows to retrieve the total light scattered in the front- and backward hemispheres with no further assumptions. The radiative transfer model used to obtain the aerosol absorption optical depth of the sample is the same as the one used in the MAAP (Petzold and Schölinner, 2004); the aerosol absorption coefficient is then calculated considering the area of the deposit and the sampled volume (Bernardoni et al. 2017; Vecchi et al. 2014).

However, the radiative transfer model by Petzold and Schölinner (2004) can be applied to the PP_UniMi data both considering the same assumptions performed by the MAAP (in which fixed values for the fraction of the back-scattered radiation by filter matrix and the asymmetry factor are imposed a-priori) or exploiting the whole available information given by the measurement of the whole phase function from the PP_UniMi (Valentini et al., 2021). Within the framework of EMEP/ACTRIS/COLOSSAL 2018 winter campaign, the PP_UniMI $b_{abs\_ref}(\lambda)$ was determined using two different approaches indicated as PP (Polar Photometer) and PaM (Photometer as MAAP). The PP approach fully exploits highly angular-resolved measurements, while PaM calculation introduces the same approximations as the ones used in the MAAP - i.e. the reconstruction (by analytical functions) from measurements at the same 3 angles and with the same fixed value between backward and total diffused radiation for blank filter (B_M=0.7) used in MAAP (Valentini et al., 2021; Bernardoni et al., 2021). It noteworthy that, recently, Valentini et al. (2021) demonstrated that by fixing B_M=0.7 affected b_{abs} obtained from MAAP with an average positive artifact of ~15%. Indeed, blank spots measured by PP_UniMI (fully exploiting highly angular-resolved measurements) showed B_M=0.88. As a consequence, Bernardoni et al. (2021) found a linear relationship between PP and MAAP, which was confirmed by Valentini et al. (2021) independently from site and season, showing an overestimation of $b_{abs}(637)$ obtained by MAAP. As reported in Bernardoni et al. (2021), at the U9 sampling site it was as:

$$b_{abs}(PP\ 635)=0.928*\ b_{abs}(MAAP\ 637)-2.07 \quad (14)$$

this equation will be used in section 3.4 to determine the time-dependent C values. Whereas an absolute and fully consistent reference method for $b_{abs}(\lambda)$ and eBC is not actually present as reported by Petzold et al. (2013), the aforementioned considerations enable to consider PP_UniMI (PP approach) as the most promising reference for $b_{abs\_ref}(\lambda)$ and C determination in the present work.

Thus, as the study aims at determining the response of the HR values as function of all the possible variations of the C values (in wavelength and in time), the following nomenclature will be applied to C:

1- C_{fix} indicates fixed values of C determined at 660 nm and applied to all AE wavelengths without any time-dependency, obtained using either MAAP (comparisons at high time resolution) or PP_UniMI (PP and PaM approaches) as reference systems

2- C_{λ} indicates wavelength-dependent C values obtained from 370 to 950 nm (not varying in time) by a comparison with the multi-λ PP_UniMI $b_{abs}(\lambda)$ reference system (section 2.3; PP approach).

3- C_t indicates time-dependent C values obtained at 660 nm by comparison with MAAP corrected data (eq. 13)

4- C_{λ_t} finally indicates wavelength- and time-dependent C values by applying the wavelength-dependence of C_{λ} (found at point 2) to the time-dependent C_t values (point 3).

Among the aforementioned C, the wavelength-dependent C_{λ} determination needs to be clarified (details are reported in Bernardoni et al., 2021). In fact, PP_UniMI, measures $b_{abs}(\lambda)$ at four wavelengths (405, 532, 635 and 780 nm) while both AE31 and AE33 works at seven wavelengths (370, 470, 520, 590, 660, 880 and 950 nm) not coincident with those of PP_UniMI. Thus, for the aim of the present paper PP_UniMI data were reported to Aethalometer wavelengths finding the best experimental absorption Ångström exponent for each sample (multi-λ fit of the four $b_{abs}(\lambda)$ as $b_{abs}(\lambda) = A\lambda^{-AAE}$ for both PP and PaM approaches) and applying it to derive $b_{abs}(\lambda)$ at all Aethalometer wavelengths with the following generic relationships:

$$b_{abs}(\lambda_{AE}) = b_{abs}(\lambda_{PP\_UniMI}) \left(\frac{\lambda_{AE}}{\lambda_{PP\_UniMI}}\right)^{-\mathrm{AAE}} \quad (15)$$

where λ_{AE} and λ_{PP_UniMI} are each pair of the nearest couple of Aethalometer and PP_UniMI wavelengths (e.g. 470 and 405 nm, 660 and 635 nm, etc.).

3. Results and discussions

Results are presented describing first the environmental context of atmospheric pollution during the campaign (section 3.1); next, sections 3.2, 3.3 and 3.4 present the HR values (total and apportioned to different species and sources of LAA) as a function of C_{fix}, C_{λ}, C_t, and C_{λ_t}. Conclusions follow with a best practice procedure for Aethalometer correction for radiative forcing assessment purposes. All the data are reported hereinafter as mean±95% confidence interval. All times are reported in local solar time (LST).

3.1 Environmental context

Highly-time resolved eBC (880 nm) loading corrected data recorded during the campaign (by both AE31 and AE33) are reported in Figure 2 together with $PM_{2.5}$ concentrations, N, wind speed, temperature and relative humidity. At the beginning of the campaign, a Föen event (4 m s^{-1} wind, 30°N) cleared the atmosphere bringing the concentrations to negligible eBC and $PM_{2.5}$ values; after this event stable atmospheric conditions occurred favoring a pollution accumulation within the mixing layer; in fact, eBC concentrations ranged from close to zero (~20 ng m^{-3}) up to 16.27 µg m^{-3}; similarly, $PM_{2.5}$ concentrations ranged from 1.6 up to 88.3 µg m^{-3} with an average value of 30.9±0.4 µg m^{-3}. The large pollution range poses the EMEP2018 COLOSSAL campaign in a good position both for C determination in different conditions (Bernardoni et al., 2021) and for the quantification of the LAA (and related $b_{abs}(\lambda)$) impact on the HR, with broader implications for any radiative transfer computation.

Figure 2 showed that eBC data, by both AE31 and AE33, were well correlated, leading to the same environmental eBC trend along time, thus appearing in good agreement (considering the different principle of operations, filter tape and constant attenuation/absorption cross sections of AE31 and AE33) for environmental monitoring purposes (and long term data series continuity). More in detail, results showed just slightly higher eBC readings (~10%) obtained from AE33 raw data; the average eBC concentrations were 3.47±0.05 µg m^{-3} (AE31) and 3.81±0.05 µg m^{-3} (AE33) being statistically different at 95% confidence level. This feature can be evidenced both with the boxplot reported in Figure 3a, and with the linear regression reported in Figure 3b: it shows high correlation ($R^2 = 0.977$) with a slope slightly higher than one (1.049±0.003) and a negligible intercept (0.073±0.015 µg m^{-3}).

The diurnal pattern of eBC (averaged between AE31 and AE33, given the above results) is reported in Figure 4a-b, together with that of $PM_{2.5}$, N, wind speed, temperature and relative humidity. The eBC, N and $PM_{2.5}$ experienced a morning peak (rush hour, 4.61±0.12 µg m^{-3}, $26 \cdot 10^3$±666 cm^{-3} and 32.2±0.9 µg m^{-3}, respectively) followed by a decrease of 45, 44 and 17% during the mid-afternoon (2.56±0.08 µg m^{-3}, $14.6 \cdot 10^3$±284 cm^{-3} and 26.8±1.1 µg m^{-3}, respectively) (Figure 4a); conversely the wind speed and temperature increased, with double values compared to morning time (Figure 4b) thus increasing atmospheric dispersion potential as typically reported in previous studies (Ferrero et al., 2011, 2019a; Carbone et al., 2010, Diemoz et al., 2019, Vecchi et al., 2019).

Within the aforementioned environmental context, the following sections investigate the impact of C_{fix}, C_{λ}, C_t, and C_{λ_t} on the HR determination in function of species and sources of LAA.

3.2 C_{fix} and resulting heating rate

3.2.1 C_{fix} values

The multiple scattering parameters C_{fix} were obtained using different instruments as reference. They were determined by comparing the AE31 and AE33 loading-corrected attenuation coefficients (b_{ATN_LC}) at 660 nm with the absorption coefficient measured: 1) by MAAP and 2) PP_UniMI, in both cases with no further wavelength adjustment (section 2.3).

The parameters C_{fix} obtained by a direct 5-min time-resolved comparison with MAAP were 3.43±0.01 and 2.64±0.01 for AE31 and AE33 respectively. The AE31 value is comparable with 3.50±0.25 suggested by GAW (2016) and with the expected range in Milan during wintertime recently reported in Ferrero et al. (2021): 3.20±0.35. The similarity between the obtained C value (3.43±0.01) and the GAW one confirms that Milan (in the middle of the Po Valley) is characterized by continental type aerosols (e.g.

Carbone et al., 2010) and that the Milan value is consistent with the global average as already verified in Ferrero et al. (2021).

The parameters C_{fix} was also determined by a comparison with PP_UniMI $b_{abs\_ref}(\lambda)$ using both the PP and PaM approaches (PP: full angular resolution; PaM: three angles as MAAP; section 2.3; Bernardoni et al., 2021) considering both all the available data ("all") and for daytime ("day") data only. Isolation of daytime data was performed as HR is determined considering aerosol-radiation interaction, which occurs only during daytime, due to radiation absence during night-time. Table 1 resumes all the results also including the traditional values for the instruments and tape in use: C_{AE31}=2.14 (Weingartner et al., 2003) and C_{AE33}= 1.57 (Drinovec et al., 2015), for further comparison on the HR data (see below). It is noteworthy that the C_{fix} obtained by a comparison with PP_UniMI under the PP approach for AE31 (4.30±0.07 and 4.44±0.11, all day and daytime, respectively) and AE33 (3.37±0.05 and 3.43±0.08, all day and daytime, respectively) were higher than the corresponding values obtained by a comparison with both PP_UniMI under the PaM approach and the ones obtained by a direct 5-min time-resolved comparison with MAAP. Thus, C_{fix_PaM} were comparable with C_{fix_MAAP} while C_{fix_PP} were 21% higher than C_{fix_PaM}. This is in agreement with results reported by Valentini et al. (2021) and recalled in section 2.3; assumptions made in the MAAP lead to higher $b_{abs\_ref}(\lambda)$ and thus lower C_{fix} (eq. 13) compared to PP approach.

Daytime values were higher than all day ones (and, consequently, they are higher than night-time results) for both aethalometers. This may be due to two different causes: a different aerosol size distributions and single scattering albedo (SSA). We begin with the role of different size distribution. A higher fraction of bigger particles can change the scattering properties of the aerosol deposited on the filter matrix. In this respect, the daytime (06:00-18:00 local solar time) and night-time (18:00-06:00 local solar time) average number size distribution measured by optical particle counter (OPC Grimm 1.107) showed a difference for particle size > 5.0 µm optical equivalent diameter (Figure S1). Ferrero et al. (2014) showed that 5.0 µm optical equivalent diameter (measured by an OPC Grimm 1.107) corresponds to an ambient geometric size of 5.9 µm, in Milan during wintertime. Thus, as the experimental set-up for the COLOSSAL winter

2018 campaign was equipped with PM2.5 cutoff inlet (Bernardoni et al., 2021), the size distribution differences observed in the coarse size range between daytime and night-time is expected to have a negligible effect.The second cause, a different SSA, is instead more reliable. Thus, this aspect was investigated given the findings reported in Collaud Coen et al. (2010) which defined the C values in function of the aerosol single scattering albedo (SSA) as follows:

$$C = C_{ref} + \alpha \frac{SSA}{1-SSA} \quad (16)$$

where C_{ref} is the reference value of C for the AE31 tape (determined in the pristine atmosphere of Jungfraujoch and Hohenpeissenberg sites where aerosol has a single scattering albedo of ~1; C_{ref} was equal to 2.81±0.11), α is the parameter for the Arnott (2005) scattering correction (0.0713 at 660 nm).

From the aforementioned statement, it is clear that the analysis can be carried out on the AE31 C data only; nonetheless, being the SSA and intrinsic property of the aerosol, the results also allow the interpretation of AE33 C data. Moreover, as Collaud Coen et al. (2010) derived C_{ref} from a comparison with MAAP data, eq. 16 was applied to PaM (section 2.3) C daytime and night-time values to derive the corresponding SSA.

By inverting eq. 16, the retrieval of SSA from the experimental C and C_{ref} led to a SSA value of 0.92±0.01 during daytime, 0.02±0.01 higher than the 0.90±0.01 SSA during night-time. The same day to night SSA difference (0.02±0.01) can also be achieved by using eq. 1 on high-time resolution C_t data (section 3.4) obtained by a direct AE31-MAAP comparison. As the SSA is related to change in the aerosol chemical composition and especially in the aerosol fraction due to the eBC, the daytime and night-time eBC fraction in $PM_{2.5}$ was investigated. Results showed a percentage of eBC in $PM_{2.5}$ of 11.9±0.3% and 12.7±0.3% (being statistically different at 95% of confidence) during daytime and night-time respectively; they are in keeping with the aforementioned SSA behaviour. Finally, the total number concentration data (N) were also used to evaluate the N/eBC ratio (Rodríguez and Cuevas, 2007; Reche et al., 2011; Dall'Osto et al., 2011, 2013; Ferrero et al., 2016). The highest values of the N/eBC ratio are expected to occur during secondary aerosol formation in the atmosphere (Reche et al., 2011) which enhance the aerosol scattering, thus lowering the SSA (Ferrero et al., 2011a; 2014). N/eBC were 5.58±0.04 and 4.86±0.04 $cm^{-3}\ ng^{-1}\ m^3$ during daytime and night-time, respectively.

Finally, due to Aethalometer type and filter differences all the C_{fix} values found for AE31 were 30% higher than the corresponding for AE33.

3.2.2 C_{fix} and total HR assessment

The different C_{fix} values will impact the determination of the HR, as described by eq. 1 (section 2.1). To this purpose, in the C_{fix} case only, eq. 1 can be rewritten as follows:

$$HR = \frac{1}{C_{fix}} \cdot \frac{1}{\rho C_p} \cdot \sum_{n=1}^{3} \int_{\theta} \int_{\lambda} \frac{F_{n(\lambda,\theta)}}{cos\theta} b_{ATN\_LC(\lambda)} d\lambda d\theta \quad (17)$$

thus showing that, once the HR with a C_{fix} value has been determined, it is possible to rescale the data using a different C_{fix} and easily to determine the HR. This represents a simple application for long-term data series harmonization of radiative forcing and HR. Thus, all HR data with all possible C_{fix} estimates were obtained by applying eq. 17; they are resumed in Table 1 where HR values range from 0.58±0.02 up to 1.21±0.05 K day^{-1} for AE31 and from 0.61±0.02 up to 1.34±0.05 K day^{-1} for AE33 (relative variability above 100%). These data are reported in Figure 5a which excludes the extremes C_{fix} values of 2.14 (Weingartner et al., 2003) and 1.57 (Drinovec et al., 2015) for AE31 and AE33, respectively, which should not be used for $b_{abs}(\lambda)$ determination from AE31 and AE33 (they are anyway reported in Table 1 and included in Figure S2). When these extremes C_{fix} values (2.14 and 1.57) are excluded, by applying all the C_{fix} obtained with the other approaches, all the HR determination are constrained within a ΔHR of 0.17±0.04 and 0.18±0.04 K day^{-1} (for AE31 and AE33) which turns into an ambient climatic error within ~30% at maximum.

If the reference C_{fix} values determined from PP at 660 nm are used, the best estimates for the AE31 and AE33 HRs become: 0.58 ± 0.02 K day^{-1} and 0.61 ± 0.02 K day^{-1}, respectively. This HR data obtained using the PP C_{fix} were the lowest obtained among all the data reported in Table 1 and Figure 5a. In fact, the HR are overestimated by a 23±6% and 31±6% factor (for AE31 and AE33) if the C_{fix} values obtained by the PaM approach and high-resolution MAAP are considered as reference, respectively.

Thus, two consequences can be highlighted from these results for the total HR:

1- Consistency: the total HR determined for each of the C_{fix} pair obtained for the two aethalometers with the same reference device/approach presented average values not statistically different at 95% probability.

2- Over-estimation: if MAAP/PaM is chosen as reference instead of a PP approach, the HR can be overestimated by 23-30% factor.

Both results can be considered site-independent and discussed as follows:

1- Consistency: this property is important for long-term data series in which e.g. the AE31 is supplanted by the AE33. Due to the absence of standard reference material for eBC and to the lack of gold standard instrumentation for the measurement of ambient aerosol absorption coefficient, at the current state of the art, the consistency refers to the reproducibility between the total HR, obtained using the AE31 and AE33, not to the accuracy. To obtain the consistency (i.e. reproducibility), it is necessary that, for both AE31 and AE33, the C_{fix} values are obtained with the same reference device (e.g. a MAAP, a photoacoustic, polar photometer) at the same time; it is important that the temporal length of overlapping in the calibration with the reference device covers all the possible aerosol scenarios (i.e. chemical composition) in the different seasons (over the investigated site) to obtain a temporal consistency. This makes the consistency property site-independent.

2- Over-estimation: this happens if MAAP/PaM is chosen as reference instead of a PP approach. This observation completes the one related to the consistency as it refers to the accuracy of the total HR in function of the reference device used to derive the C factor applied to the Aethalometers (AE31 and AE33). It is noteworthy that the MAAP is a widely accepted reference device in the scientific community. Nevertheless, Valentini et al. (2021) derived a relationship between the MAAP absorption coefficient (that is obtained with limitation of imposing: 3 fixed angles, the backscattered fraction from blank filter at 0.7 and the asymmetry factor at 0.75) and the one obtained from the PP_UniMI (that allows to retrieve the total light scattered in the front- and backward hemispheres with no further assumptions – thus in principle improving measurement accuracy). This relationship was derived considering aerosol sampled at different urban and regional background sites in southern Europe, by a comparison between MAAP data and PP_UniMI analysis of the MAAP spots collected during the MAAP measurements. Thus, we expect that the relationship found by Valentini et al. (2021) has wide applicability (it generalizes eq. 14, section 2.3, which instead is valid only for the Milan case). Such relationship is:

$$b_{abs}(PP)=0.86(\pm 0.01)*b_{abs}(MAAP)-0.19(\pm 0.03) \quad (18)$$

where the absorption coefficient b_{abs} is expressed in Mm^{-1}. Thus, once MAAP data are available in each site, they can be converted in the corresponding PP values enabling to improve the accuracy of b_{abs} determination and thus that of the total HR.

The possibility to solve the over-estimation of the total HR is important as the HR quantification will reflect on the assessment of the atmospheric feedbacks related to the HR; for example, the influence on the liquid water content (Jacobson et al., 2002), planetary boundary layer dynamics (Su et al., 2020; Ferrero et al., 2014), regional circulation systems (Ramanathan and Carmichael, 2008; Ramanathan and Feng, 2009) and cloud dynamic and evolution itself (Koren et al., 2008; Bond et al., 2013). Thus, any arbitrary, not verified, use of C_{fix} will also be reflected in the modelled HR-triggered feedbacks with the aforementioned uncertainty range of ~30% (at minimum, if climatic amplification phenomena in the triggered feedbacks are not present).

Finally, the all vs. day C_{fix} impact on the HR reported in Table 1 highlighted that the use of a day-time C_{fix} turns into a total HR that was 3.4% lower with respect to that obtained using the whole day ("all") C_{fix}. A detailed discussion on this topic is included in section 3.4.

Here below, the impact of using a wavelength independent C_{fix} on the HR apportionment between FF and BB and between BC and BrC contribution is discussed.

3.2.3 C_{fix} and HR apportionment

The previous results reported for the total HR highlighted the possibility to obtain a temporal consistency in long-term data series. Conversely, the data analysis showed a different scenario when the LAA sources (FF and BB) and speciation (BC and BrC) are considered by using the "Aethalometer model" (Sandradewi et al., 2008a) or the method proposed by Tian et al. (2019) (section 2.1). Their values are resumed in Figure 5b (for PP C_{fix} daytime data only) and in Table 1 for all the C_{fix} used above.

Focusing on the single C_{fix} calculation approach for data correction, HR_{FF} obtained by the AE33 data showed higher values (+24±1%; +0.10±0.02 K day^{-1}) than that of AE31; conversely, HR_{BB} for AE33 was -28±1% (-0.08±0.01 K day^{-1}) lower than for AE31. When the LAA species (BC and BrC) were apportioned, AE33 HR_{BC} values were higher (+0.06±0.01 K day^{-1}; +10±1%) than for AE31, and HR_{BrC} for AE33 was -29±1% (-0.03±0.01 K day^{-1}) lower than for AE31. These variations reflect on the corresponding contribution of FF/BB/BC/BrC to the total HR. In this respect, HR_{FF} and HR_{BB} accounted for 60±3% and 40±2% in the AE31 data series, while for AE33 their contribution changed to 72±4% and 28±2%, respectively. A similar behavior was observed for the LAA speciation, with the HR_{BC} and HR_{BrC} contribution of 85±5% and 15±3% in the AE31 data and of 91±5% and 9±1% in the AE33 data, respectively.

The reasons behind these behaviours lie in the $b_{abs}(\lambda)$ spectra of AE31 and AE33 that, once C_{fix} is applied, differ at the extreme wavelengths: 370 and 950 nm (Figure 6a). These differences are respectively of 4% and 6% (1.5 and 0.7 Mm^{-1}), with higher values measured by the AE33. Between the two wavelengths, the highest one (950 nm) affects the classical apportionment methods (the "Aethalometer model" and the BrC determination by Tian et al., 2019) while the lowest one (370 nm) affects the increase of the AAE of the source/species. In this respect, Figure 6b-e report the average $b_{abs}(\lambda)$ spectra (from both AE31 and AE33) for FF, BB, BC and BrC obtained using the classical apportionment methods: they are in agreement with the HR apportionment differences described above. To explain the phenomenon, it is necessary to recall that, when the HR is determined (eq. 1-2), $b_{abs}(\lambda)$ is integrated over the whole aethalometer spectrum. In this respect, the FF and BC b_{abs} integrals were 15±4 and 6±4% higher for AE33 when compared to AE31.

Conversely, the BB and BrC integrals were -23±4 and -26±4% lower for AE33 when compared to AE31. As the HR (eq. 1-2) is determined as an integral over the whole absorption spectrum, even a small bias on $b_{abs}(950)$ can be magnified (after the application of the "Aethalometer model" and the BrC determination by Tian et al., 2019) by the integral operator on the obtained source and species $b_{abs}(\lambda)$ which are reported in Figure 6b-e.

From the aforementioned results, two important consequences can be derived for the HR apportionment (sources and species):

1- Inconsistency in long temporal series when a C_{fix} value is used and older AE31 are replaced by the new AE33. This inconsistency generates when the traditional source (FF and BB) and speciation (BC and BrC) apportionment models ("Aethalometer model" and the Tian et al. (2019) method) are considered. The HR_{FF}, HR_{BB} and HR_{BrC} presented average values statistically different at 95% probability when determined from the two aethalometers with C_{fix} obtained with the same reference device. The only exception is given by HR_{BC} probably because BC accounts for the large majority of LAA in the atmosphere.

2- Over-estimation for the AE33 concerning HR_{FF} and HR_{BC} (and vice versa for HR_{BB} and HR_{BrC}) relative to the AE31. This poses an important issue concerning the long-term quantification of the HR improvement due to the policies implemented in the context of climate change mitigation.

Therefore, consistent HR source apportionment/speciation approaches are discussed in the next section.

3.3 Overcoming the inconsistencies in HR source and speciation apportionment

As mentioned in the previous section, the inconsistency (between AE31 and AE33) of the HR source and speciation apportionment represents an important issue, especially when long-term data series are considered in the context of climatic change.

Two approaches can be used to overreach this problem:

1- by introducing a wavelength dependent C_{λ} parameter for each aethalometer type using PP_UniMI (PP approach) as a reference instrument, 2- by smoothing out the role of extreme wavelengths using all the $b_{abs}(\lambda)$ information (based on C_{fix}) and applying multi-λ regression fitting as "multi-λ fit" and MWAA described in section 2.1.

As shown in the following, these approaches are alternative and not counteracting, and they feature both advantages and disadvantages.

3.3.1 C_λ and HR apportionment

C_λ data, obtained using the methodology reported in section 2.3, are reported in Table 2. When the wavelength dependent parameters C_λ are applied, by definition the total $b_{abs}(\lambda)$ spectra agrees for the AE31 and AE33 (Figure 6f), as all wavelengths of the same instrument are reported to the same value. As a consequence, the application of both the "Aethalometer model" and Tian et al. (2019) method becomes consistent between AE31 to AE33 (Figure 6g-l), with negligible differences even when $b_{abs}(\lambda)$ is integrated over the aethalometer spectrum (1/10 of the differences compared to the case in which a fixed correction C_{fix} is applied). The obtained results (in terms of HR) are resumed in Table 1 and Figure 7. First, using C_λ with traditional source and speciation apportionment approaches, the total HR value lies at 0.59±0.02 K day^{-1} for both AE31 and AE33, resulting in a consistent temporal evolution in a climate change monitoring scenario. With respect to the HR source apportionment, HR_{FF} and HR_{BB} became 0.40±0.02 and 0.42±0.02 K day^{-1}, and 0.19±0.01 and 0.17±0.01 K day^{-1} (AE31 and AE33). The speciated HR_{BC} became 0.53±0.02 and 0.54±0.02 K day^{-1}, and HR_{BrC} 0.06±0.01 and 0.06±0.01 K day^{-1} (AE31 and AE33), respectively. These results demonstrate the need for using accurate wavelength dependent multiple scattering parameters C_λ; this is important especially when the source apportionment "Aethalometer model" and speciation (Tian et al., 2019) models are used. Obviously, there is the need to determine proper C_λ values using appropriate reference methods.

3.3.2 Application of multi-wavelength models

The second approach to overcome the inconsistency shown in section 3.2.3 is to use advanced models: the "multi-λ fit" and MWAA apportionment models recalled in section 2.1 (Bernardoni et al., 2021;

Massabò et al., 2015). In this case, their application (Table 1 and Figure 7), based on the appropriate PP daytime C_{fix}, resulted in a HR_{FF} of 0.39±0.02 K day^{-1} (both AE31 and AE33) and in a HR_{BB} of 0.19±0.01 and 0.21±0.01 K day^{-1} (AE31 and AE33); in the light of HR speciation, the MWAA resulted in HR_{BC} of 0.46±0.02 and 0.53±0.02 K day^{-1}, and HR_{BrC} of 0.14±0.01 and 0.09±0.01 K day^{-1} (AE31 and AE33). Finally, the total HR did not vary with respect to previous section, being again 0.58±0.02 and 0.61±0.02 K day^{-1} for AE31 and AE33, respectively. The aforementioned data demonstrate the consistency for FF/BB apportionment, while the MWAA application from AE31 to AE33 by using a simple C_{fix} generates a discrepancy up to 58% when considering the BrC. However the AE33 HR_{BrC} (0.09±0.01 K day^{-1}) was in keeping with the values obtained in section 3.3.2 using the Tian et al. (2019) method.

It is noteworthy, however, that while the wavelength dependent C_{λ} values obtained for each aethalometer type are a site-dependent result, that need to be investigated in other sites and seasons around the world (to this aim, multi-wavelength reference information is needed), the use of multi-λ regression fitting and MWAA (Massabò et al., 2015), with care and limitations to BrC apportionment (as above mentioned) can be applied worldwide with no need of further instrumentation and check.

3.3.3 Comparison with literature data

The obtained results (sections 3.3.1 and 3.3.2 and Table 2) can be compared with similar studies concerning both the C values and the related effect on radiative transfer. The C values of the Aethalometer AE31 (resumed in Table 1) obtained using the MAAP/PaM reference are close to that reported in Weingartner et al. (2003) (3.66±1.53 and 3.90±1.13) referring to its experiment in smog chamber when soot particles were internally mixed with organic matter that in Milan accounts for more than 35% in winter (Perrone et al., 2012; Ferrero et al., 2019a) due to the aged nature of the Po Valley aerosol. Arnott et al. (2005) arrived to a similar conclusion addressing a C=3.69 as the most suitable for ambient measurements in urban sites. Schmid et al. (2006) found AE31 C values up to 4.0-4.4 for internally mixed aerosol (e.g., for aged ambient aerosol), very close to the C_{λ} PP range (4.27-4.63) reported in the present work and detailed in Bernardoni et al. (2021). For what concerns the Aethalometer AE33 C values, a recent work of Valentini et al. (2021) reported a C value (at 660 nm) of 2.66 (on M8060 filter material) using the PaM reference, while Yus-Díez et al. (2021) investigated the C_λ dependency, finding it statistically significant for aged aerosol in the range of 3.47-4.03.

Finally, Rajesh and Ramachandran (2018) recently investigated the aerosol absorption coefficients obtained from AE31 and AE33 using C=2.14 and C=1.57 (Weingartner et al., 2003 and Drinovec et al., 2015), the aerosol SSA, and their role on the radiative forcing. They showed an average difference of 28% between AE31 and AE33 absorption coefficients. These differences, when not corrected (as instead done in the present work) can lead to an aerosol radiative forcing perturbation changing the estimation of the atmospheric warming up to 25%.

As a final conclusion, these results and the comparison with literature ones point towards the direction of both 1) using of multi-λ regression fitting and MWAA approaches (limited to BC) to improve the HR apportionment and 2) exploring on a global scale the wavelength dependent multiple scattering correction factors (C_λ) and their effect on climate forcing apportionment determination.

3.4 The temporal variation of *C* and the heating rate

3.4.1 C_t features

As highlighted in section 3.2, there was a ~4% difference between HRs determined using C_{fix} values obtained on the whole dataset and on daytime data only. To further investigate this difference, temporally-resolved multiple scattering coefficients C_t were obtained for each hour of day by comparing the AE31 and AE33 data (b_{ATN_LC}) at 660 nm with the absorption coefficient (b_{abs}) measured by the MAAP (rescaled to the PP reference as detailed in section 2.3, eq. 14). This step was performed for consistency with the C_{fix} values chosen as reference in section 3.2.

Figure 8 shows the daily behavior of the multiple scattering parameters C_t for AE31 and AE33. Daily trends of C_t for both AE31 and AE33 were characterized by two peaks, one in the morning (6:00-8:00

LST) and one in the afternoon (17:00-19:00 LST) roughly in correspondence of the rush hours. C_t of AE31 presented a maximum variation of 9% (range: 4.21 - 4.59), while for the C_t of AE33 is of 6% constrained in a narrower range: 3.31- 3.51. The reason behind the presence of the two peaks (e.g. change in chemical composition) is beyond the aim of the present paper; the possible artifacts related to negligible relative humidity variations were avoided due to the presence of dryers which turned into an absence of relationship with the daily variation of ambient RH (Figure S3). An insight into the possible explanation of the C_t daily trend comes from the observation of the trend of N/eBC ratio. Results demonstrated that also the N/eBC ratio experienced the same two peaks, the one in the morning (6:00-8:00 LST) and the one in the afternoon (17:00-19:00 LST): 5.78±0.14 and 6.11±0.12 cm^{-3} ng^{-1} m^3, respectively. This suggests that a higher fraction of scattering aerosol (primary or secondary) in the atmosphere can be responsible of the observed correction of the multiple scattering parameter at the same time-slots.

3.4.2 Total HR and its apportionment considering C temporal variability

In order to obtain a proper time-dependent investigation of the total HR and its apportionment (FF, BB, BC and BrC) the time-independent C_λ values were used to generate a C_{λ_t} correction by following the relative trend of C_t in Figure 8 (as in section 3.3 it has been demonstrated the need for a wavelength dependent multiple scattering correction factors in order to obtain a consistent source/species apportionment of LAA using the Aethalometer model and the Tian et al., 2019 method). Moreover, the C_t values were applied for using the Multi-λ fit and the MWAA methods.

Figures 9a-l resumes the obtained HR and its daily average source and speciation apportionment considering different C calculation approaches for both AE31 and AE33; Figure 10a-d reports the linear correlation (AE33 vs. AE31) of the HR daily apportionment (FF, BB, BC and BrC) by using the Aethalometer model and the Tian et al. (2019) method on the basis of both time-dependent C_t and C_{λ_t} correction and by using the Multi-λ fit and the MWAA methods on the basis of the time-dependent C_t.

Figures 9a and 9f show that for both AE31 and AE33 total HR, the interaction between eBC concentration and the radiation intensity (Figures 4a-b) resulted in an asymmetric temporal behavior (with respect to midday) characterized by a HR peak between the rush hour and midday (~10 LST; 1.04±0.02 and 1.01±0.02 K day^{-1} peaks for AE31 and AE33, respectively) followed by a constant decrease until sunset. Such behavior appears very important for understanding atmospheric feedbacks induced by the HR, e.g. the influence on the planetary boundary layer evolution during the morning and on the aerosol liquid water content (when morning fog events may dissipate). This asymmetric temporal behavior of total HR is due to the synergy between the eBC concentration featuring a morning peak (Figure 4a) and F_{glo} showing larger values at midday (Figure 4b). Indeed, the amount of available radiation increased in the late morning and early afternoon while the eBC concentrations decreased, leading to a compensatory effect. It noteworthy that the F_{glo} radiation curve peaked when C_t reached minimum values. Thus, the impact of C_t variability (9% and 6% for AE31 and AE33, respectively) on total HRs and their apportionment from both instruments is here below investigated.

In this respect, Figures 9a-l show that the daily cycle of total HR average values (together with HR_{FF}, HR_{BB}, HR_{BC} and HR_{BrC}) did not statistically differ at 95% probability when the AE31/AE33 instrument and the apportionment method are fixed. In other words, the daily trend is unaffected by the use of fixed or time-varying C values. In addition to this, the linear correlations reported in Figure 10a-b demonstrate, even along the diurnal cycle, that the HR_{FF} and HR_{BB} reached the maximum agreement between the two Aethalometers (slopes close to 1, R^2>0.98) only when a wavelength- and time-dependent multiple scattering parameters $C_{\lambda,t}$ was used for the application of the "Aethalometer model" or when C_t is applied together with the "multi-λ fit" apportionment method, in keeping with Figure 7 and Table 1. Similarly, Figure 10c-d demonstrate, even along the diurnal cycle, that the HR_{BC} and HR_{BrC} reached the maximum agreement (slopes close to 1, R^2>0.98) only when wavelength- and time-dependent multiple scattering parameters $C_{\lambda,t}$ are used with the Tian et al., 2019 model, in keeping with Figure 7 and Table 1. Instead, the MWAA model application (Figure 10c-d) generates a discrepancy up to 17% considering the BC and of about 50% for BrC, as already discussed in section 3.4. As a final remark, it noteworthy that the C_t impact on the HR should be investigated in the future in different locations, especially far from midlatitudes (e.g. northern Europe, Arctic and Antarctica), where the diurnal cycle of sunshine and anthropogenic/natural LAA source can be very different.

Conclusions

Experimental heating rate (HR) values were obtained in the Po Valley (Milan), in the framework of the EMEP/ACTRIS/COLOSSAL 2018 winter campaign, using the Aethalometers AE31 and AE33. Source (fossil fuel, FF and biomass burning, BB) and speciation (black and brown carbon, BC and BrC) apportionment models were applied to derive the corresponding heating rates: HR_{FF}, HR_{BB}, HR_{BC} and HR_{BrC}.

The effect of different wavelength- and time-dependent multiple scattering parameters (C) on the HRs was investigated using different filter photometers (PP_UniMI and MAAP) as reference.

As a conclusion, the best practices for accurate and temporally consistent HR data (from Aethalometers AE31/AE33) are resumed here below:

1) The use of single wavelength- and time-independent value of *C* (i.e. C_{fix} at 660 nm) results in temporally consistent total HR data between AE31 and AE33 version. However, this correction approach also results in statistically significant biases in the source (FF, BB) and speciation (BC and BrC) apportionment of the HR between the AE31 and the AE33, when traditional apportionment methods ("Aethalometer model" and Tian et al., 2019 model) are used. If not accounted for, these biases could give a false impression of ambient changes in terms of climate forcing due to different sources or nature of LAA when long-term data series in which AE33 supplanted AE31 are analysed. To overcome this problem, whenever further investigation on the *C* wavelength-dependence is not possible, advanced source and species apportionment methods (Multi-λ fit or MWAA) have to be applied to obtain more consistent results, with limitation with respect to the HR_{BrC} from MWAA.

2) The use of a wavelength dependent multiple scattering correction parameters C_{λ} with traditional apportionments methods overcome all the aforementioned problems, generating a fully consistent dataset of HR (together with HR_{FF}, HR_{BB}, HR_{BC} and HR_{BrC}). Nevertheless, C_{λ} determination requires the

availability multi-wavelength absorption measurements by a reference instrument in the season and sampling site of interest.

3) The use of a time dependent multiple scattering correction parameter C_t, at the latitude of Milan, has a negligible impact on the total HR, and its source/species apportionment.

Acknowledgements

This work is an output of the GEMMA Center in the framework of project MIUR "Dipartimenti di Eccellenza 2018-2022".

This work was carried out in the frame of the activities of the COST-COLOSSAL action CA16109 Chemical On-Line cOmpoSition and Source Apportionment of fine aerosol.

This work was partially funded by the National Institute of Nuclear Physics (INFN), in the frame of the INFN-TRACCIA experiment.

The authors want to acknowledge Aerosol d.o.o and LSI-Lastem for supporting the experimental campaign.

Appendix A: Nomenclature

Nomenclature

Aerosol Acronyms

AAE	Absorption Angstrom Exponent
AAE_{BC}	Absorption Angstrom Exponent of Black Carbon
AAE_{BrC}	Absorption Angstrom Exponent of Brown Carbon
ATN	Attenuation
$b_{abs}(\lambda)$	wavelength dependent aerosol absorption coefficient (Mm^{-1})
$b_{abs\_ref}(\lambda)$	wavelength dependent aerosol absorption coefficient from reference system (Mm^{-1})
$b_{ATN}(\lambda)$	wavelength dependent aerosol attenuation coefficient (Mm^{-1})
$b_{ATN\_LC}(\lambda)$	wavelength dependent aerosol attenuation coefficient corrected for loading (Mm^{-1})
C_{fix}	multiple scattering correction parameter at 660 nm, time independent
C_λ	wavelength dependent multiple scattering correction parameter, time independent
C_t	time dependent multiple scattering correction parameter at 660 nm

$C_{\lambda,t}$	wavelength and time dependent multiple scattering correction parameter
BB	Biomass Burning
BC	Black Carbon
BrC	Brown Carbon
eBC	equivalent Black Carbon concentration (µg m^{-3}) (Petzold et al., 2013)
FF	Fossil Fuel
LAA	Light Absorbing Aerosol
HR	Heating Rate (K day^{-1})
HR_{BB}	Heating Rate of Biomass Burning (K day^{-1})
HR_{BC}	Heating Rate of Black Carbon (K day^{-1})
HR_{BrC}	Heating Rate of Brown Carbon (K day^{-1})
HR_{FF}	Heating Rate of Fossil Fuel (K day^{-1})
N	Total particle number concentration d > 4 nm (cm^{-3})
PaM	Photometer as MAAP
PP	Polar Photometer
R(ATN)	Loading correction parameter
SSA	Single Scattering Albedo

Other Symbols/Acronyms

α	Arnott (2005) scattering parameter
ϕ	Azimuth angle (rad)
λ	Wavelength (nm)
ρ	Air Density (kg m^{-3})
θ	Zenith angle (rad)
θ_z	Solar zenith angle (rad)
C_p	Isobaric specific heat of dry air (1005 J kg^{-1} K^{-1})
dif	diffuse
dir	direct
F_{glo}	Global broadband irradiance; $F_{glo} = F_{dir} + F_{dif}$ (W m^{-2})
F_{dif}	Diffuse broadband irradiance (W m^{-2})
F_{dir}	Direct broadband irradiance (W m^{-2})
F_{ref}	Reflected broadband irradiance (W m^{-2})
$F_{dir,dif,ref}(\lambda)$	Spectral irradiance in function of λ (W m^{-2} nm^{-1})
ref	reflected

References

Andreae, M., and Ramanathan, V. 2013. Climate's Dark Forcings, Science, 340(2002), 280–281, doi:10.1126/science.1235731.

Arnott, W. P., Hamasha, K., Moosmüller, H., Sheridan, P. J. and Ogren, J., 2005. Towards Aerosol Light-Absorption Measurements with a 7-Wavelength Aethalometer: Evaluation with a Photoacoustic Instrument and 3-Wavelength Nephelometer. Aerosol Science and Technology, 39(1), 17–29, doi:10.1080/027868290901972.

Arnott, W.P., Moosmueller, H., Rogers, C.F., Jin, T., Bruch, T., 1999. Photoacoustic spectrometer for measuring light absorption by aerosol: instrument description. Atmospheric Environment, 33, 2845-2852, https://doi.org/10.1016/S1352-2310(98)00361-6.

Barnaba, F. and Gobbi, G. P., 2004. Aerosol seasonal variability over the Mediterranean region and relative impact of maritime, continental and Saharan dust particles over the basin from MODIS data in the year 2001. Atmospheric Chemistry and Physics, 4(9/10), 2367–2391, doi:10.5194/acp-4-2367-2004.

Bernardoni, V., Ferrero, L., Bolzacchini, E., Forello, A.C., Gregorič, A., Massabò, D., Močnik, G., Prati, P., Rigler, M., Santagostini, L., Soldan, F., Valentini, S., Valli, G., Vecchi, R., 2021. Determination of Aethalometer multiple-scattering enhancement parameters and impact on source apportionment during the winter 2017–2018 EMEP/ACTRIS/COLOSSAL campaign in Milan. Atmos. Meas. Tech., 14, 2919–2940. https://doi.org/10.5194/amt-14-2919-2021

Bernardoni, V., Valli, G., Vecchi, R., 2017. Set-up of a multi wavelength polar photometer for off-line absorption coefficient measurements on 1-h resolved aerosol samples. Journal of Aerosol Science, 107, 84–93. https://doi.org/10.1016/j.jaerosci.2017.02.009.

Bond, T. C., Anderson, T. L., Campbell, D., 1999. Calibration and intercomparison of filter-based measurements of visible light absorption by aerosols. Aerosol Sci. Tech., 30(6), 582–600.

Bond, T. C., Doherty, S. J., Fahey, D. W., Forster, P. M., Berntsen, T., Deangelo, B. J., Flanner, M. G., Ghan, S., Kärcher, B., Koch, D., Kinne, S., Kondo, Y. and Quinn, P. K., 2013. Bounding the role of black carbon in the climate system : A scientific assessment. Journal of Geophysical Research, 118, 1–173, doi:10.1002/jgrd.50171.

Burciaga, U.M.: Sustainability Assessment in Housing Building Organizations for the Design of Strategies against Climate Change, HighTech and Innovation Journal, 1(4), 136–147, doi:10.28991/hij-2020-01-04-01, 2020.

Cape, J. N.; Coyle, M.; Dumitrean, P. The atmospheric lifetime of black carbon. Atmos. Environ. 2012, 59, 256−263.

Carbone, C., Decesari, S., Mircea, M., Giulianelli, L., Finessi, E., Rinaldi, M., Fuzzi, S., Marinoni, A., Duchi, R., Perrino, C., Sargolini, T., Vardè, M., Sprovieri, F., Gobbi, G. P., Angelini, F., and Facchini, M. C., 2010. Size-resolved aerosol chemical composition over the Italian Peninsula during typical summer and winter conditions. Atmos. Environ., 44, 5269–5278, doi:10.1016/j.atmosenv.2010.08.008.

Chung, C. E., Ramanathan, V. and Decremer, D., 2012. Observationally constrained estimates of carbonaceous aerosol radiative forcing., Proceedings of the National Academy of Sciences of the United States of America, 109(29), 11624–9, doi:10.1073/pnas.1203707109.

Cogliati, S., Rossini, M., Julitta, T., Meroni, M., Schickling, A., Burkart, A., Pinto, F., Rascher, U., Colombo, R., 2015. Continuous and long-term measurements of reflectance and sun-induced chlorophyll fluorescence by using novel automated field spectroscopy systems. Remote Sensing of Environment, 164, 270–281, http://dx.doi.org/10.1016/j.rse.2015.03.027.

Collaud Coen M., Weingartner E., Apituley A., Ceburnis D., Fierz-Schmidhauser R., Flentje H., Henzing J.S., Jennings S.G., Moerman M., Petzold A., Schmid O., Baltensperger U., 2010. Minimizing light absorption measurement artifacts of the Aethalometer: evaluation of five correction algorithms. Atmos. Meas. Tech., 3, 457–474.

Costabile, F., Barnaba, F., Angelini, F. and Gobbi, G. P., 2013. Identification of key aerosol populations through their size and composition resolved spectral scattering and absorption, Atmospheric Chemistry and Physics, 13(5), 2455–2470, doi:10.5194/acp-13-2455-2013.

Črnivec, N. and Mayer, B., 2019. Quantifying the bias of radiative heating rates in numerical weather prediction models for shallow cumulus clouds, Atmospheric Chemistry and Physics, 19(12), 8083–8100, doi:10.5194/acp-19-8083-2019.

Crova, F., Valli, G., Bernardoni, V., Forello, A.C., Valentini, S., Vecchi, R., 2021. Effectiveness of airborne radon progeny assessment for atmospheric studies, Atmospheric Research, 250, 105390, doi: 10.1016/j.atmosres.2020.105390.

Dall'Osto, M., Querol, X., Alastuey, A., O'Dowd, C., Harrison, R.M., Wenger, J., and Gómez-Moreno, F. J., 2013. On the spatial distribution and evolution of ultrafine particles in Barcelona, Atmos. Chem. Phys., 13, 741–759, doi:10.5194/acp-13-741-2013.

Dall'Osto, M., Thorpe, A., Beddows, D. C. S., Harrison, R. M., Barlow, J. F., Dunbar, T., Williams, P. I., and Coe, H., 2011. Remark-able dynamics of nanoparticles in the urban atmosphere, Atmos. Chem. Phys., 11, 6623–6637, doi:10.5194/acp-11-6623-2011.

Di Nicolantonio, W., Cacciari, A., Bolzacchini, E., Ferrero, L., Volta, M., and Pisoni, E., 2007. MODIS aerosol optical properties over north Italy for estimating surface-level PM2.5, Proc. Envisat Symposium 2007, Montreux, Switzerland, 23–27 April 2007 (ESA SP-636, July 2007), http://envisat.esa.int/envisatsymposium/proceedings/posters/3P5/464392wd.pdf.

Di Nicolantonio, W., Cacciari, A., Petritoli, A., Carnevale, C., Pisoni, E., Volta, M. L., Stocchi, P., Curci, G., Bolzacchini, E., Ferrero, L., Ananasso, C., and Tomasi, C., 2009. MODIS and OMI satellite observations supporting air quality monitoring, Radiat. Prot. Dosim., 137(3–4), 280–287.

Diémoz, H., Barnaba, F., Magri, T., Pession, G., Dionisi, D., Pittavino, S., Tombolato, I. K. F., Campanelli, M., Ceca, L. S. Della, Hervo, M., Di Liberto, L., Ferrero, L. and Gobbi, G. P., 2019. Transport of Po Valley aerosol pollution to the northwestern Alps-Part 1: Phenomenology, Atmospheric Chemistry and Physics, 19(5), 3065–3095, doi:10.5194/acp-19-3065-2019.

Drinovec, L., Mocnik, G., Zotter, P., Prevot, A. S. H., Ruckstuhl, C., Coz, E., Rupakheti, M., Sciare, J., Müller, T., Wiedensohler, A. and Hansen, A.D.A., 2015. The "dual-spot" Aethalometer: An improved measurement of aerosol black carbon with real-time loading compensation, Atmospheric Measurement Techniques, 8(5), 1965–1979, doi:10.5194/amt-8-1965-2015.

Eleftheriadis, K., Vratolis, S. and Nyeki, S., 2009. Aerosol black carbon in the European Arctic: Measurements at Zeppelin station, Ny-Ålesund, Svalbard from 1998-2007, Geophysical Research Letters, 36(2), doi:10.1029/2008GL035741.

Ferrero L., Močnik G., Cogliati S., Gregorič A., Colombo R., Bolzacchini E., 2018. Heating Rate of Light Absorbing Aerosols: Time-Resolved Measurements, the Role of Clouds, and Source Identification. Environ. Sci. Tech., 52, 3546−3555, DOI: 10.1021/acs.est.7b04320.

Ferrero, L., Cappelletti, D., Busetto, M., Mazzola, M., Lupi, A., Lanconelli, C., Becagli, S., Traversi, R., Caiazzo, L., Giardi, F., Moroni, B., Crocchianti, S., Fierz, M., Mocnik, G., Sangiorgi, G., Perrone, M.G., Maturilli, M., Vitale, V., Udisti, R., Bolzacchini, E., 2016. Vertical profiles of aerosol and black carbon in the Arctic: a seasonal phenomenology along 2 years (2011–2012) of field campaigns, Atmos. Chem. Phys., 16(19), 12601–12629, https://doi.org/10.5194/acp-16-12601-2016.

Ferrero, L., Cappelletti, D., Moroni, B., Sangiorgi, G., Perrone, M. G., Crocchianti, S. and Bolzacchini, E., 2012. Wintertime aerosol dynamics and chemical composition across the mixing layer over basin valleys, Atmospheric Environment, 56, 143–153, doi:10.1016/j.atmosenv.2012.03.071.

Ferrero, L., Castelli, M., Ferrini, B.S., Moscatelli, M., Perrone, M.G., Sangiorgi, G., Rovelli, G., D'Angelo, L., Moroni, B., Scardazza, F., Mocnik, G., Bolzacchini, E., Petitta, M., Cappelletti, D., 2014. Impact of Black Carbon Aerosol over Italian basin valleys: high resolution measurements along vertical profiles, radiative forcing and heating rate. Atmos. Chem. Phys., 14, 9641–9664.

Ferrero, L., Gregorič, A., Močnik, G., Rigler, M., Cogliati, S., Barnaba, F., Di Liberto, L., Gobbi, G.P., Losi, N., Bolzacchini, E., 2021. The impact of cloudiness and cloud type on the atmospheric heating rate of black and brown carbon, Atmos. Chem. Phys., 21, 4869–4897. https://doi.org/10.5194/acp-21-4869-2021.

Ferrero, L., Mocnik, G., Ferrini, B.S., Perrone, M.G., Sangiorgi, G., Bolzacchini, E., 2011a. Vertical profiles of aerosol absorption coefficient from micro-Aethalometer data and Mie calculation over Milan. Sci. Total Environ. 409 (14), 2824–2837. https://doi.org/ 10.1016/j.scitotenv.2011.04.022.

Ferrero, L., Riccio, a., Perrone, M. G., Sangiorgi, G., Ferrini, B. S. and Bolzacchini, E., 2011b. Mixing height determination by tethered balloon-based particle soundings and modeling simulations, Atmospheric Research, 102(1–2), 145–156, doi:10.1016/j.atmosres.2011.06.016.

Ferrero, L., Riccio, A., Ferrini, B. S., D'Angelo, L., Rovelli, G., Casati, M., Angelini, F., Barnaba, F., Gobbi, G. P., Cataldi, M. and Bolzacchini, E., 2019a. Satellite AOD conversion into ground PM10, PM2.5 and PM1 over the Po valley (Milan, Italy) exploiting information on aerosol vertical profiles, chemistry, hygroscopicity and meteorology, Atmospheric Pollution Research, 10(6), 1895–1912, doi:10.1016/j.apr.2019.08.003.

Ferrero, L., Ritter, C., Cappelletti, D., Moroni, B., Močnik, G., Mazzola, M., Lupi, A., Becagli, S., Traversi, R., Cataldi, M., Neuber, R., Vitale, V., Bolzacchini, E., 2019b. Aerosol optical properties in the Arctic: the role of aerosol chemistry and dust composition in a closure experiment between Lidar and tethered balloon vertical profiles. Sci. Tot. Environ., 686, 452–467, doi.org/10.1016/j.scitotenv.2019.05.399.

Gao, R. S., Hall, S. R., Swartz, W. H., Schwarz, J. P., Spackman, J. R., Watts, L. A., Fahey, D. W., Aikin, K. C., Shetter, R. E. and Bui, T. P., 2008. Calculations of solar shortwave heating rates due to black carbon and ozone absorption using in situ measurements, Journal of Geophysical Research Atmospheres, 113(14), 14–19, doi:10.1029/2007JD009358.

GAW Report No. 227, 2016. WMO/GAW Aerosol Measurement Procedures, Guidelines and Recommendations, 2nd Edition. ISBN 978-92-63-11177-7.

Huang, J., Fu, Q., Su, J., Tang, Q., Minnis, P., Hu, Y., Yi, Y. and Zhao, Q., 2009. Taklimakan dust aerosol radiative heating derived from CALIPSO observations using the Fu-Liou radiation model with CERES constraints, Atmospheric Chemistry and Physics Discussions, 9(2), 5967–6001, doi:10.5194/acpd-9-5967-2009.

IPCC, 2013: Climate Change 2013: The Physical Science Basis. Cambridge University Press, Cambridge, United Kingdom and New York, USA.

Jacobson, M. Z., 2002. Control of fossil-fuel particulate black carbon and organic matter, possibly the most effective method of slowing global warming. J. Geophys. Res., 107 (D19), 4410.

Jacobson, M. Z.: Short-term effects of controlling fossil-fuel soot, biofuel soot and gases, and methane on climate, arctic ice, and air pollution health, J. Geophys. Res., 115, D14209, doi:10.1029/2009JD013795, 2010.

Javadinejad, S., Dara, R. and Jafary, F.: Climate change scenarios and effects on snow-melt runoff, Civil Engineering Journal (Iran), 6(9), 1715–1725, doi:10.28991/cej-2020-03091577, 2020.

Junker, C., Jennings, S. G., and Cachier, H., 2006. Aerosol light absorption in the North Atlantic: trends and seasonal characteristics during the period 1989 to 2003. Atmos. Chem. Phys., 6, 1913– 1925.

Kaufman, Y.J., Tanré, D., Boucher, O., 2002. A satellite view of aerosols in the climate system. Nature 419, 215–223, 2002.

Kibaara, S. K., Murage, D. K., Musau, P. and Saulo, M. J.: Comparative Analysis of Implementation of Solar PV Systems Using the Advanced SPECA Modelling Tool and HOMER Software: Kenyan Scenario, HighTech and Innovation Journal, 1(1), 8–20, doi:10.28991/hij-2020-01-01-02, 2020.

Kirchstetter, T. W., Novakov, T. and Hobbs, P.V., 2004. Evidence that the spectral dependence of light absorption by aerosols is affected by organic carbon, Journal of Geophysical Research D: Atmospheres, 109(21), 1–12, doi:10.1029/2004JD004999.

Koch, D., Del Genio, A.D., 2010. Black carbon semi-direct effects on cloud cover: review and synthesis. Atmos. Chem. Phys. 10, 7685–7696, doi:10.5194/acp-10-7685-2010.

Koch, D., Schulz, M., Kinne, S., Mcnaughton, C., Spackman, J. R., Balkanski, Y., Bauer, S. and Berntsen, T., 2009. Evaluation of black carbon estimations in global aerosol models. Atmospheric Chemistry and Physics (November), 9001–9026.

Koren, I., Kaufman, Y.J., Remer, L.A., Martins, J.V., 2004. Measurments of the effect of amazon smoke on inhibition of cloud formation. Scienze, 303, 1342-1345.

Koren, I., Martins, J.V., Remer, L.A., Afargan, H., 2008. Smoke invigoration versus inhibition of clouds over the amazon, Science, 321, 946-949.

Laskin, A., Laskin, J. and Nizkorodov, S. A., 2015. Chemistry of Atmospheric Brown Carbon, Chemical Reviews, 115(10), 4335–4382, doi:10.1021/cr5006167.

Lemaître, C., Flamant, C., Cuesta, J., Raut, J. C., Chazette, P., Formenti, P. and Pelon, J., 2010. Radiative heating rates profiles associated with a springtime case of Bodélé and Sudan dust transport over West Africa, Atmospheric Chemistry and Physics, 10(17), 8131–8150, doi:10.5194/acp-10-8131-2010.

Liousse, C., Cachier, H., Jennings, S. G., 1993. Optical and thermal measurements of black carbon aerosol content in different environments: Variation of the specific attenuation cross-section, sigma (σ). Atmospheric Environment, 27(8), 1203–1211.

Mallet, M., Tulet, P. and Serc, D., 2009. Impact of dust aerosols on the radiative budget , surface heat fluxes , heating rate profiles and convective activity over West Africa during March 2006. Atmospheric Chemistry and Physics, 9, 7143–7160.

Massabò, D., Caponi, L., Bernardoni, V., Bove, M. C., Brotto, P., Calzolai,, G., Cassola, F., Chiari, M., Fedi, M. E., Fermo, P., Gi- annoni, M., Lucarelli, F., Nava, S., Piazzalunga, A., Valli, G., Vecchi, R., Prati, P., 2015. Multi-wavelength optical determination of black and brown carbon in atmospheric aerosols, Atmos. Environ., 108, 1–12.

Matus, A.V., L'Ecuyer, T.S., Kay, J.E., Hannay, C. and Lamarque, J.F., 2015. The role of clouds in modulating global aerosol direct radiative effects in spaceborne active observations and the community earth system model, Journal of Climate, 28(8), 2986–3003, doi:10.1175/JCLI-D-14-00426.1.

Moosmüller, H., Chakrabarty, R. K. and Arnott, W. P., 2009. Aerosol light absorption and its measurement: A review, Journal of Quantitative Spectroscopy and Radiative Transfer, 110(11), 844–878, doi:10.1016/j.jqsrt.2009.02.035, 2009.

Moosmüller, H., Chakrabarty, R. K., Ehlers, K. M., and Arnott, W. P., 2011. Absorption Ångström coefficient, brown carbon, and aerosols: basic concepts, bulk matter, and spherical particles, Atmos. Chem. Phys., 11, 1217–1225, doi:10.5194/acp-11-1217- 2011.

Müller, T., Henzing, J. S., de Leeuw, G., Wiedensohler, A., Alastuey, A., Angelov, H., Bizjak, M., Collaud Coen, M., Engström, J. E., Gruening, C., Hillamo, R., Hoffer, A., Imre, K., Ivanow, P., Jennings, G., Sun, J. Y., Kalivitis, N., Karlsson, H., Komppula, M., Laj, P., Li, S.-M., Lunder, C., Marinoni, A., Martins dos Santos, S., Moerman, M., Nowak, A., Ogren, J. A., Petzold, A., Pichon, J. M., Rodriquez, S., Sharma, S., Sheridan, P. J., Teinilä, K., Tuch, T., Viana, M., Virkkula, A., Weingartner, E., Wilhelm, R., Wang, Y. Q., 2011. Characterization and intercomparison of aerosol absorption photometers: result of two intercomparison workshops, Atmospheric Measurement Techniques, 4, 245–268, doi.org/10.5194/amt-4-245-2011.

Müller, T., Henzing, J. S., De Leeuw, G., Wiedensohler, A., Alastuey, A., Angelov, H., Bizjak, M., Collaud Coen, M., Engström, J. E., Gruening, C., Hillamo, R., Hoffer, A., Imre, K., Ivanow, P., Jennings, G., Sun, J. Y., Kalivitis, N., Karlsson, H., Komppula, M., Laj, P., Li, S. M., Lunder, C., Marinoni, A., Martins Dos Santos, S., Moerman, M., Nowak, A., Ogren, J. A., Petzold, A., Pichon, J. M., Rodriquez, S., Sharma, S., Sheridan, P. J., Teinilä, K., Tuch, T., Viana, M., Virkkula, A., Weingartner, E., Wilhelm, R. and Wang, Y. Q., 2011. Characterization and intercomparison of aerosol absorption photometers: Result of two intercomparison workshops, Atmospheric Measurement Techniques, 4(2), 245–268, doi:10.5194/amt-4-245-2011.

Myhre, G., Samset, B. H., Schulz, M., Balkanski, Y., Bauer, S., Berntsen, T. K., Bian, H., Bellouin, N., Chin, M., Diehl, T., Easter, R. C., Feichter, J., Ghan, S. J., Hauglustaine, D., Iversen, T., Kinne, S., Kirkeväg, A., Lamarque, J. F., Lin, G., Liu, X., Lund, M. T., Luo, G., Ma, X., Van Noije, T., Penner, J. E., Rasch, P. J., Ruiz, A., Seland, Skeie, R. B., Stier, P., Takemura, T., Tsigaridis, K., Wang, P., Wang, Z., Xu, L., Yu, H., Yu, F., Yoon, J. H., Zhang, K., Zhang, H. and Zhou, C., 2013. Radiative forcing of the direct aerosol effect from AeroCom Phase II simulations, Atmospheric Chemistry and Physics, 13(4), 1853–1877, doi:10.5194/acp-13-1853-2013.

Nordmann, S., Cheng, Y. F., Carmichael, G. R., M. Yu, M., Denier van der Gon, H. A. C., Zhang, Q., Saide, P. E., Pöschl, U., Su, H., Birmili, W., Wiedensohler, A., 2014. Atmospheric black carbon and warming effects influenced by the source and absorption enhancement in central Europe. Atmos. Chem. Phys., 14, 12683–12699, doi:10.5194/acp-14-12683-2014.

Ødemark, K., Dalsøren, S. B., Samset, B. H., Berntsen, T. K., Fu- glestvedt, J. S., and Myhre, G., 2012 Short-lived climate forcers from current shipping and petroleum activities in the Arctic, Atmos. Chem. Phys., 12, 1979–1993, doi:10.5194/acp-12-1979-2012.

Oo, H. T., Zin, W. W. and Thin Kyi, C. C.: Analysis of streamflow response to changing climate conditions using SWAT model, Civil Engineering Journal (Iran), 6(2), 194–209, doi:10.28991/cej-2020-03091464, 2020.

Petzold, A., Kopp, C., Niessner, R., 1997. The dependence of the specific attenuation cross-section on black carbon mass fraction and particle size. Atmospheric Environment, 31(5), 661–672.

Petzold, A., Ogren, J. A., Fiebig, M., Laj, P., Li, S.-M., Baltensperger, U., Holzer-Popp, T., Kinne, S., Pappalardo, G., Sugimoto, N., Wehrli, C., Wiedensohler, A., and Zhang, X.-Y., 2013. Recommendations for reporting "black carbon" measurements. Atmos. Chem. Phys., 13, 8365–8379, https://doi.org/10.5194/acp-13-8365-2013.

Petzold, A., Schloesser, H., Sheridan, P.J., Arnott, W.P., Ogren, J.A., Virkkula, A., 2005. Evaluation of Multiangle Absorption Photometry for Measuring Aerosol Light Absorption. Aerosol Science and Technology, 39, 40–51.

Petzold, A., Schönlinner, M., 2004. Multi-angle absorption photometry—A new method for the measurement of aerosol light absorption and atmospheric black carbon. Journal of Aerosol Science, 35, 421–441, doi.org/10.1016/j.jaerosci.2003.09.005.

Qerimi, D., Dimitrieska, C., Vasilevska, S. and Rrecaj, A.: Modeling of the solar thermal energy use in urban areas, Civil Engineering Journal (Iran), 6(7), 1349–1367, doi:10.28991/cej-2020-03091553, 2020.

Quinn, P.K., Bates, T.S., Baum, E., Doubleday, N., Fiore, A.M., Flanner, M., Fridlind, A., Garrett, T.J., Koch, D., Menon, S., Shindell, D., Stohl, A., Warren, S.G., 2008. Short-lived pollutants in the Arctic: their climate impact and possible mitigation strategies. Atmos. Chem. Phys. 8, 1723–1735. https://doi.org/10.5194/acp-8-1723-2008.

Rajesh, T.A., Ramachandran, S., 2018. Black carbon aerosol mass concentration, absorption and single scattering albedo from single and dual spot aethalometers: Radiative implications. Journal of Aerosol Science 119, 77–90. doi:10.1016/j.jaerosci.2018.02.001

Ramanathan, V. and Feng, Y., 2009. Air pollution, greenhouse gases and climate change: Global and regional perspectives, Atmos. Environ., 43(1), 37–50, doi:10.1016/j.atmosenv.2008.09.063.

Ramanathan, V., Carmichael, G., 2008. Global and regional climate changes due to black carbon. Nat. Geosci., 1, 221–227.

Ran, L., Deng, Z., Xu, X., Yan, P., Lin, W., Wang, Y., Tian, P., Wang, P., Pan, W. and Lu, D., 2016. Vertical profiles of black carbon measured by a micro-aethalometer in summer in the North China Plain, Atmospheric Chemistry and Physics, 16(16), 10441–10454, doi:10.5194/acp-16-10441-2016.

Reche, C., Querol, X., Alastuey, A., Viana, M., Pey, J., Moreno, T., Rodríguez, S., González, Y., Fernández-Camacho, R., de la Rosa, J., Dall'Osto, M., Prévôt, A. S. H., Hueglin, C., Harrison, R. M., and Quincey, P., 2011. New considerations for PM, Black Carbon and particle number concentration for air quality monitoring across different European cities, Atmos. Chem. Phys., 11, 6207–6227, doi:10.5194/acp-11-6207-2011.

Rodrıguez, S. and Cuevas, E., 2007. The contributions of "minimum primary emissions" and "new particle formation enhancements" to the particle number concentration in urban air, J. Aerosol Sci., 38, 1207–1219, doi:10.1016/j.jaerosci.2007.09.001.

Samset, B. H., Stjern, C. W., Andrews, E., Kahn, R. A., Myhre, G., Schulz, M. and Schuster, G. L., 2018. Aerosol Absorption: Progress Towards Global and Regional Constraints, Current Climate Change Reports, 4(2), 65–83, doi:10.1007/s40641-018-0091-4.

Samset, B. H.; Myhre, G.; Schulz, M.; Balkanski, Y.; Bauer, S.; Berntsen, T. K.; Bian, H.; Bellouin, N.; Diehl, T.; Easter, R. C.; Ghan, S. J.; Iversen, T.; Kinne, S.; Kirkevåg, A.; Lamarque, J.- F.; Lin, G.; Liu, X.; Penner, J. E.; Seland, Ø.; Skeie, R. B.; Stier, P.; Takemura, T.; Tsigaridis, K.; Zhang, K. Black carbon vertical profiles strongly affect its radiative forcing uncertainty. Atmos. Chem. Phys. 2013, 13, 2423−2434.Sandradewi J., Prevot A.S.H., Szidat S., Perron N., Alfarra M.R., Lanz V.A., Weingartner E., and

Baltensperger U., 2008a. Using Aerosol Light Absorption Measurements for the Quantitative Determination of Wood Burning and Traffic Emission Contributions to Particulate Matter. Environ. Sci. Technol., 42, 3316–3323.

Sandradewi, J., Prevot, A.S.H., Weingartner, E., Schmidhauser, R., Gysel, M., Baltensperger, U., 2008b. A study of wood burning and traffic aerosols in an Alpine valley using a multi-wavelength Aethalometer. Atmos. Environ, 42, 101–112.

Schmid, O., Artaxo, P., Arnott, W. P., Chand, D., Gatti, L. V., Frank, G. P., Hoffer, a., Schnaiter, M. and Andreae, M.O., 2006. Spectral light absorption by ambient aerosols influenced by biomass burning in the Amazon Basin. I: Comparison and field calibration of absorption measurement techniques, Atmospheric Chemistry and Physics, 6(11), 3443–3462, doi:10.5194/acp-6-3443-2006.

Shamjad, P. M., Tripathi, S. N., Pathak, R., Hallquist, M., Arola, A. and Bergin, M. H., 2015. Contribution of Brown Carbon to Direct Radiative Forcing over the Indo-Gangetic Plain, Environmental Science and Technology, 49(17), 10474–10481, doi:10.1021/acs.est.5b03368.

Shindell, D., Faluvegi, G., 2009. Climate response to regional radiative forcing during the twentieth century. Nat. Geosci. 2 (4), 294–300. https://doi.org/10.1038/ngeo473.

Srinivas, B. and Sarin, M. M., 2013. Light absorbing organic aerosols (brown carbon) over the tropical Indian Ocean: impact of biomass burning emissions, Environ. Res. Lett., 8, 044042, https://doi.org/10.1088/1748-9326/8/4/044042.

Su, T., Li, Z., Li, C., Li, J., Han, W., Shen, C., Tan, W., Wei, J. and Guo, J., 2020. The significant impact of aerosol vertical structure on lower atmosphere stability and its critical role in aerosol–planetary boundary layer (PBL) interactions, Atmospheric Chemistry and Physics, 20(6), 3713–3724, doi:10.5194/acp-20-3713-2020.

Tian, P., Liu, D., Zhao, D., Yu, C., Liu, Q., Huang, M., Deng, Z., Ran, L., Wu, Y., Ding, S., Hu, K., Zhao, G., Zhao, C. and Ding, D., 2019. In-situ vertical characteristics of optical properties and heating rates of aerosol over Beijing, Atmospheric Chemistry and Physics Discussions, 1–33, doi:10.5194/acp-2019-780.

Valentini, S., Bernardoni, V., Bolzacchini, E., Ciniglia, D., Ferrero, L., Forello, A.C., Massabó, D., Pandolfi, M., Prati, P., Soldan, F., Valli, G., Yus-Díez, J., Alastuey, A., Vecchi, R., 2021. Applicability of benchtop multi-wavelength polar photometers to off-line measurements of the Multi-Angle Absorption Photometer (MAAP) samples. Journal of Aerosol Science 152, 1–13. doi:10.1016/j.jaerosci.2020.105701.

Vecchi R., Bernardoni V., Paganelli C., Valli G., 2014. A filter-based light-absorption measurement with polar photometer: Effects of sampling artefacts from organic carbon. Journal of Aerosol Science, 70, 15-25, doi.org/10.1016/j.jaerosci.2013.12.012.

Vecchi, R., Marcazzan, G., Valli, G., Cerini, M., and Antoniazzi, C., 2004. The role of atmospheric dispersion in the seasonal variation of PM1 and PM2.5 concentration and composition in the urban area of Milan (Italy), Atmos. Environ., 38, 4437–4446.

Vecchi, R., Piziali, F. A., Valli, G., Favaron, M. and Bernardoni, V., 2019. Radon-based estimates of equivalent mixing layer heights: A long-term assessment, Atmospheric Environment, 197(June 2018), 150–158, doi:10.1016/j.atmosenv.2018.10.020.

Virkkula, A., 2010. Correction of the Calibration of the 3-wavelength Particle Soot Absorption Photometer (3PSAP). Aerosol Science and Technology, 44, 706–712.

Weingartner, E., Saathoff, H., Schnaiter, M., Streit, N., Bitnar, B. and Baltensperger, U., 2003. Absorption of light by soot particles: determination of the absorption coefficient by means of aethalometers, Journal of Aerosol Science, 34(10), 1445–1463, doi:10.1016/S0021-8502(03)00359-8.

Yang, M., Howell, S.G., Zhuang, J., Huebert, B.J., 2009. Attribution of aerosol light absorption to black carbon, brown carbon, and dust in China and interpretations of atmospheric measurements during EAST-AIRE. Atmospheric Chemistry and Physics, 9, 2035-2050.

Yus-Díez, J., Bernardoni, V., Močnik, G., Alastuey, A., Ciniglia, D., Ivančič, M., Querol, X., Perez, N., Reche, C., Rigler, M., Vecchi, R., Valentini, S., and Pandolfi, M., 2021. Determination of the multiple-scattering correction factor and its cross-sensitivity to scattering and wavelength dependence for different AE33 Aethalometer filter tapes: A multi-instrumental approach, Atmos. Meas. Tech. Discuss., https://doi.org/10.5194/amt-2021-46.

Figure captions

Figure 1. Flow chart of the research methodology.

Figure 2. High-time resolution time series of data for the whole EMEP/ACTRIS/COLOSSAL 2018 campaign for equivalent black carbon (eBC, from AE31 and AE33), together with wind speed, temperature, relative humidity, $PM_{2.5}$ and total particle concentrations (N).

Figure 3. AE33 vs. AE33 eBC concentrations in box-lot (a) and linear correlation (b).

Figure 4. Daily trend of eBC, total particle number (N) and $PM_{2.5}$ concentrations (a); daily trend of wind speed (WS), temperature (T) and global radiation (F_{glo}) values (b). The shaded area correspond to the confidence interval at 95%.

Figure 5. a) HR determined by using different C_{fix} values obtained from different reference (MAAP, PP all, PP day, PaM all, PaM day) for both AE31 and AE33; b) HR apportioned between Fossil Fuel (FF), Biomass Burning (BB), BC and BrC by applying the "Aethalometer model" and the Tian et al. (2019) method under the PP day C_{fix} (4.44 for AE31 and 3.43 for AE33) application to the whole $b_{abs}(\lambda)$ spectrum. The error bars represents the confidence interval at 95%.

Figure 6. Absorption coefficients ($b_{abs(\lambda)}$) for both AE31 and AE33 for the whole spectrum and its apportionment (FF, BB, BC and BrC) by using the Aethalometer model and the Tian et al. (2019) method on the basis of a single C_{fix} correction (panels from a to e); absorption coefficients ($b_{abs(\lambda)}$) for both AE31

and AE33 for the whole spectrum and its apportionment (FF, BB, BC and BrC) by using the Aethalometer model and the Tian et al. (2019) method on the basis of multi-wavelength C_{λ} correction (panels from f to l). The shaded area correspond to the confidence interval at 95%.

Figure 7. Total and apportioned HR obtained by applying different apportionment methods using the most suitable multiple scattering correction factor (C) for each method. The error bars represents the confidence interval at 95%.

Figure 8. C_t values at 660 nm obtained from MAAP reference once reported at equivalent PP ($b_{abs(PP\ 660)}$=0.928*$b_{abs(MAAP,660)}$-2.07; eq. 14, section 2.3) for both AE31 and AE33. The shaded area correspond to the confidence interval at 95%.

Figure 9. Daily trend of heating rate (HR) data for both AE31 (panels a-e, left side) and AE33 (panels f-l, right side) and its apportionment (FF, BB, BC and BrC) by using the Aethalometer model and the Tian et al. (2019) method on the basis of a time-independent C_{λ} correction or a temporal C_{λ_t} correction; the same apportionment (FF, BB, BC and BrC) is reported by using the Multi-λ fit and the MWAA methods on the basis of a time-independent PP daytime C_{fix} (4.44 for AE31 and 3.43 for AE33) correction or a temporal C_t. The shaded area correspond to the confidence interval at 95%.

Figure 10. Linear correlation (AE33 vs. AE31) of the heating rate (HR) daily trend data, apportionment (FF, BB, BC and BrC) by using the Aethalometer model and the Tian et al. (2019) method on the basis of a time-dependent C_t and C_{λ_t} correction; the same apportionment (FF, BB, BC and BrC) is reported by using the Multi-λ fit and the MWAA methods on the basis of a time-dependent PP C_t.

Table captions

Table 1. Multiple scattering correction factors C (C_{fix} and C_{λ}) with the corresponding HR values (K day^{-1}) ± the confidence interval at 95% apportioned with respect to sources (FF and BB) and species (BC and BrC) of LAA by using different models (Aethalometer model, Multi-λ fit, Tian et al., (2019), MWAA). The values that ensure a full consistency in both the total HR and its apportionment between AE31 and AE33 are highlighted in the table in bold.

Table 2. Multiple scattering C_{λ} values for all the AE31 and AE33 wavelengths (from 370 to 950 nm) during diurnal time for radiative forcing applications.

Table1

Reference		C determination	C values	HR	Aethalometer Model HR_{FF}	Aethalometer Model HR_{BB}	Multi-λ fit HR_{FF}	Multi-λ fit HR_{BB}	Tian et al. (2019) HR_{BC}	Tian et al. (2019) HR_{BrC}	MWAA HR_{BC}	MWAA HR_{BrC}
AE31	**C_{fix}**	Weingartner et al. 2003	2.14	1.21±0.05	0.75±0.03	0.49±0.02	0.81±0.04	0.4±0.02	1.06±0.04	0.19±0.04	0.94±0.04	0.29±0.02
		MAAP high res (660 nm)	3.43±0.01	0.76±0.03	0.47±0.02	0.31±0.01	0.5±0.02	0.25±0.01	0.66±0.03	0.12±0.02	0.59±0.03	0.18±0.01
		PP all (660 nm)	4.30±0.07	0.60±0.02	0.37±0.02	0.24±0.01	0.4±0.02	0.2±0.01	0.53±0.02	0.09±0.02	0.47±0.02	0.14±0.01
		PP day (660 nm)	4.44±0.11	0.58±0.02	0.36±0.02	0.24±0.01	**0.39±0.02**	**0.19±0.01**	0.51±0.02	0.09±0.02	0.46±0.02	0.14±0.01
		PaM all (660 nm)	3.56±0.04	0.73±0.03	0.45±0.02	0.30±0.01	0.49±0.02	0.24±0.01	0.64±0.03	0.11±0.02	0.57±0.02	0.17±0.01
		PaM day (660 nm)	3.65±0.07	0.71±0.03	0.44±0.02	0.29±0.01	0.47±0.02	0.23±0.01	0.62±0.03	0.11±0.02	0.55±0.02	0.17±0.01
	C_{λ}	PP day (370-950 nm; Table 2)	min-max: 4.27-4.63	**0.59±0.02**	**0.40±0.02**	**0.19±0.01**	//	//	**0.53±0.02**	**0.07±0**	//	//
AE33	**C_{fix}**	Drinovec et al. 2015	1.57	1.34±0.05	0.98±0.04	0.37±0.02	0.85±0.04	0.46±0.02	1.21±0.05	0.12±0.01	1.15±0.05	0.19±0.01
		MAAP high res (660 nm)	2.64±0.01	0.80±0.03	0.58±0.02	0.22±0.01	0.51±0.02	0.28±0.01	0.72±0.03	0.07±0	0.68±0.03	0.12±0
		PP all (660 nm)	3.37±0.05	0.62±0.02	0.46±0.02	0.17±0.01	0.4±0.02	0.22±0.01	0.56±0.02	0.06±0	0.54±0.02	0.09±0
		PP day (660 nm)	3.43±0.08	0.61±0.02	0.45±0.02	0.17±0.01	**0.39±0.02**	**0.21±0.01**	0.55±0.02	0.06±0	**0.53±0.02**	**0.09±0**
		PaM all (660 nm)	2.79±0.03	0.76±0.03	0.55±0.02	0.21±0.01	0.48±0.02	0.26±0.01	0.68±0.03	0.07±0	0.65±0.03	0.11±0
		PaM day (660 nm)	2.82±0.05	0.75±0.03	0.55±0.02	0.21±0.01	0.48±0.02	0.26±0.01	0.68±0.03	0.07±0	0.64±0.03	0.11±0

CV	PP day (370-950 nm; Table 2)	min-max: 3.41-3.78	**0.59±0.02**	**0.42±0.02**	**0.17±0.01**	//	//	**0.54±0.02**	**0.06±0**	//	//

Table2

λ (nm)	C daytime values	
	AE31	AE33
370	4.63	3.78
470	4.42	3.56
520	4.38	3.57
590	4.38	3.55
660	4.44	3.43
880	4.34	3.41
950	4.27	3.57

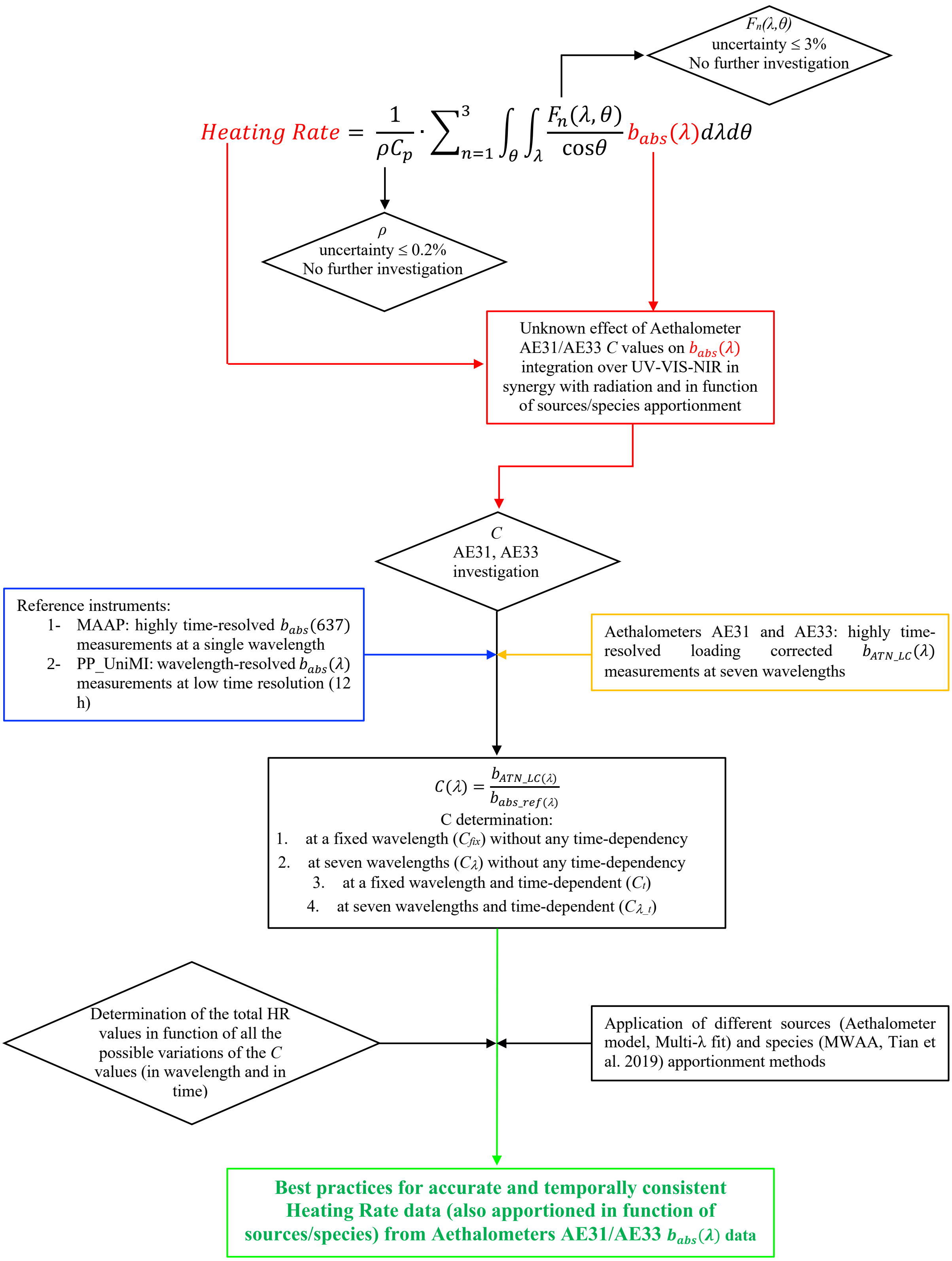
$F_n(\lambda,\theta)$
uncertainty ≤ 3%
No further investigation
$Heating\ Rate = \frac{1}{\rho C_p} \cdot \sum_{n=1}^{3} \int_{\theta} \int_{\lambda} \frac{F_n(\lambda,\theta)}{\cos\theta} b_{abs}(\lambda) d\lambda d\theta$
ρ
uncertainty ≤ 0.2%
No further investigation
Unknown effect of Aethalometer AE31/AE33 C values on $b_{abs}(\lambda)$ integration over UV-VIS-NIR in synergy with radiation and in function of sources/species apportionment
C
AE31, AE33
investigation
Reference instruments:
1- MAAP: highly time-resolved $b_{abs}(637)$ measurements at a single wavelength
2- PP_UniMI: wavelength-resolved $b_{abs}(\lambda)$ measurements at low time resolution (12 h)
Aethalometers AE31 and AE33: highly time-resolved loading corrected $b_{ATN\_LC}(\lambda)$ measurements at seven wavelengths
$C(\lambda) = \frac{b_{ATN\_LC(\lambda)}}{b_{abs\_ref(\lambda)}}$
C determination:
1. at a fixed wavelength (C_{fix}) without any time-dependency
2. at seven wavelengths (C_{λ}) without any time-dependency
3. at a fixed wavelength and time-dependent (C_t)
4. at seven wavelengths and time-dependent (C_{λ_t})
Determination of the total HR values in function of all the possible variations of the C values (in wavelength and in time)
Application of different sources (Aethalometer model, Multi-λ fit) and species (MWAA, Tian et al. 2019) apportionment methods
Best practices for accurate and temporally consistent Heating Rate data (also apportioned in function of sources/species) from Aethalometers AE31/AE33 $b_{abs}(\lambda)$ data

Figure2 Click here to access/download;Figure;Figure_FV2.pdf

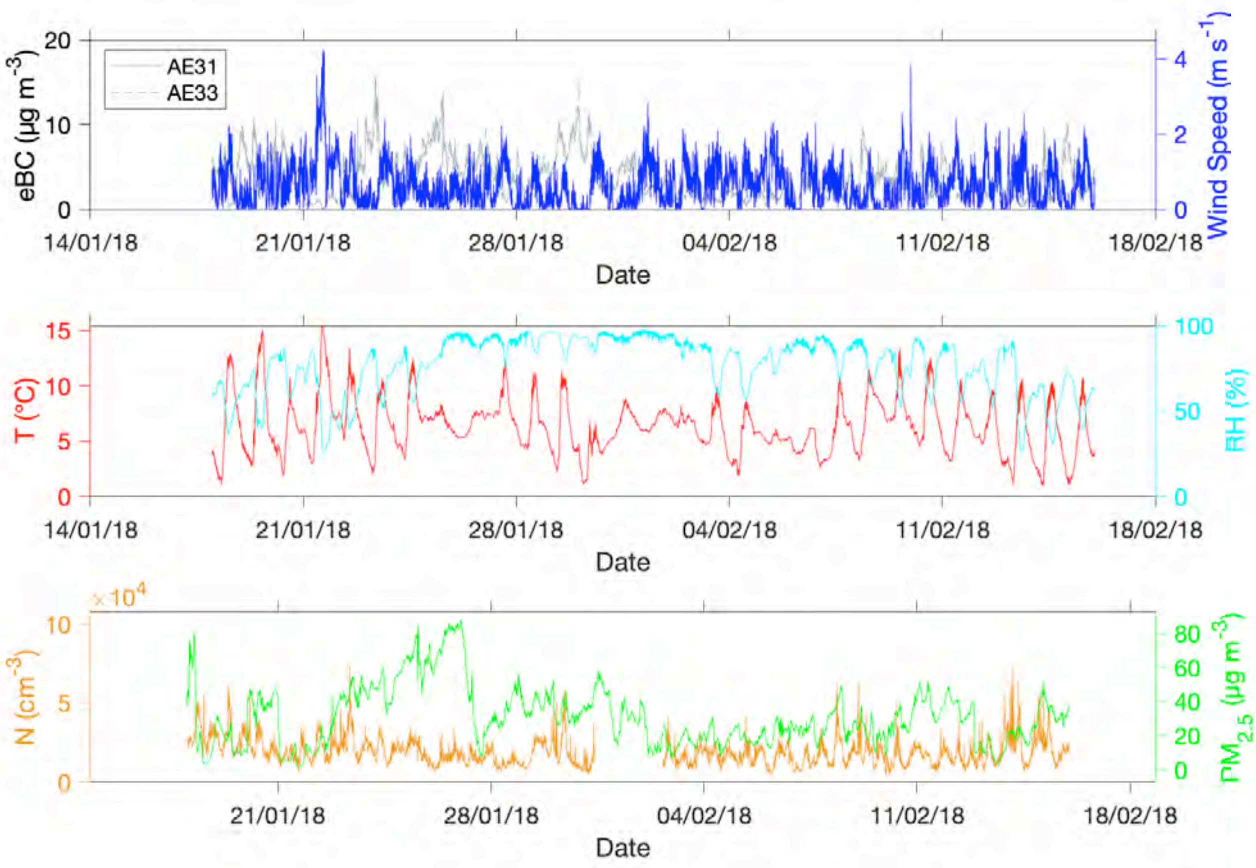

Figure3

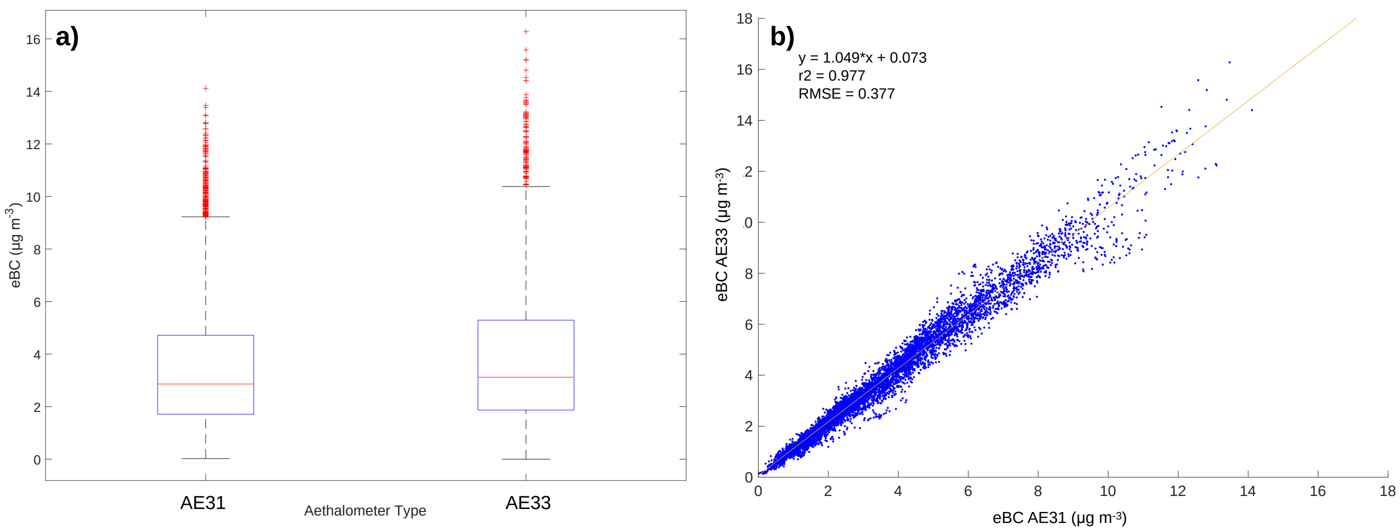
a)
eBC (μg m-3)
16
14
12
10
8
6
4
2
0
AE31
Aethalometer Type
AE33
b)
y = 1.049*x + 0.073
r2 = 0.977
RMSE = 0.377
eBC AE33 (μg m-3)
eBC AE31 (μg m-3)
18
16
14
12
10
8
6
4
2
0

Figure4 Click here to access/download;Figure;Figure_FV4.pdf

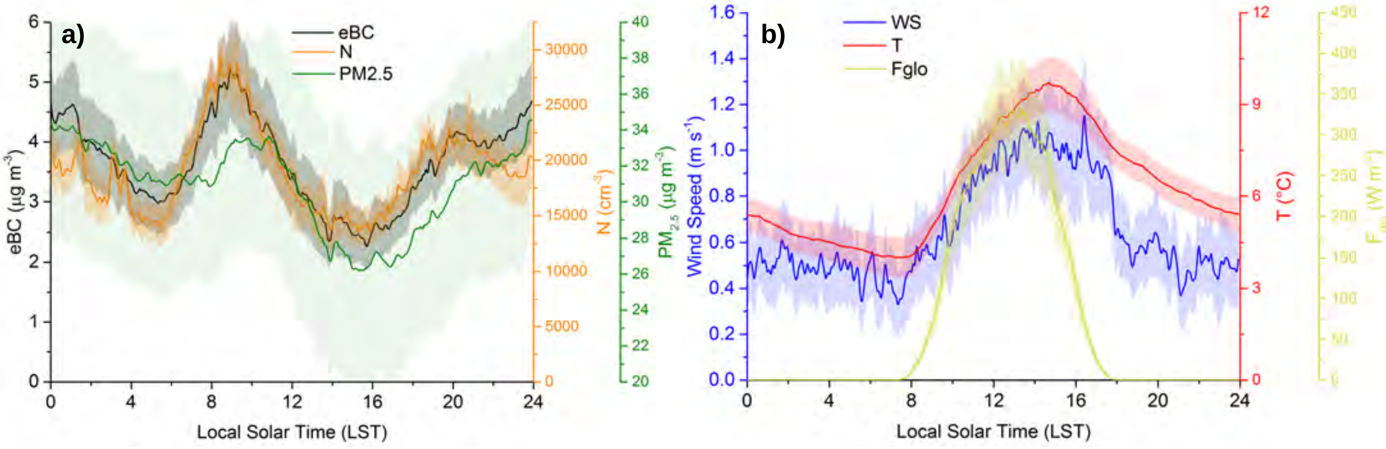

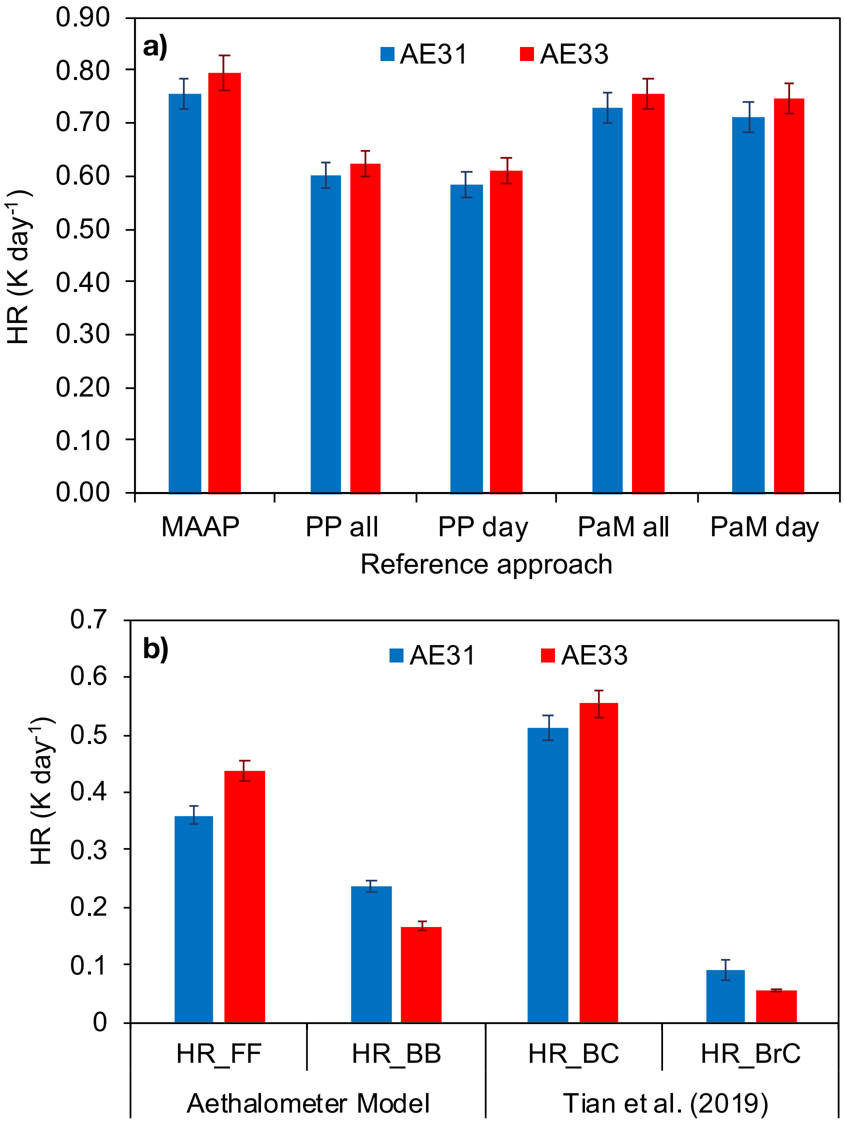
a)
AE31
AE33
HR (K day⁻¹)
0.90
0.80
0.70
0.60
0.50
0.40
0.30
0.20
0.10
0.00
MAAP
PP all
PP day
PaM all
PaM day
Reference approach
b)
AE31
AE33
HR (K day⁻¹)
0.7
0.6
0.5
0.4
0.3
0.2
0.1
0
HR_FF
HR_BB
HR_BC
HR_BrC
Aethalometer Model
Tian et al. (2019)

Figure6

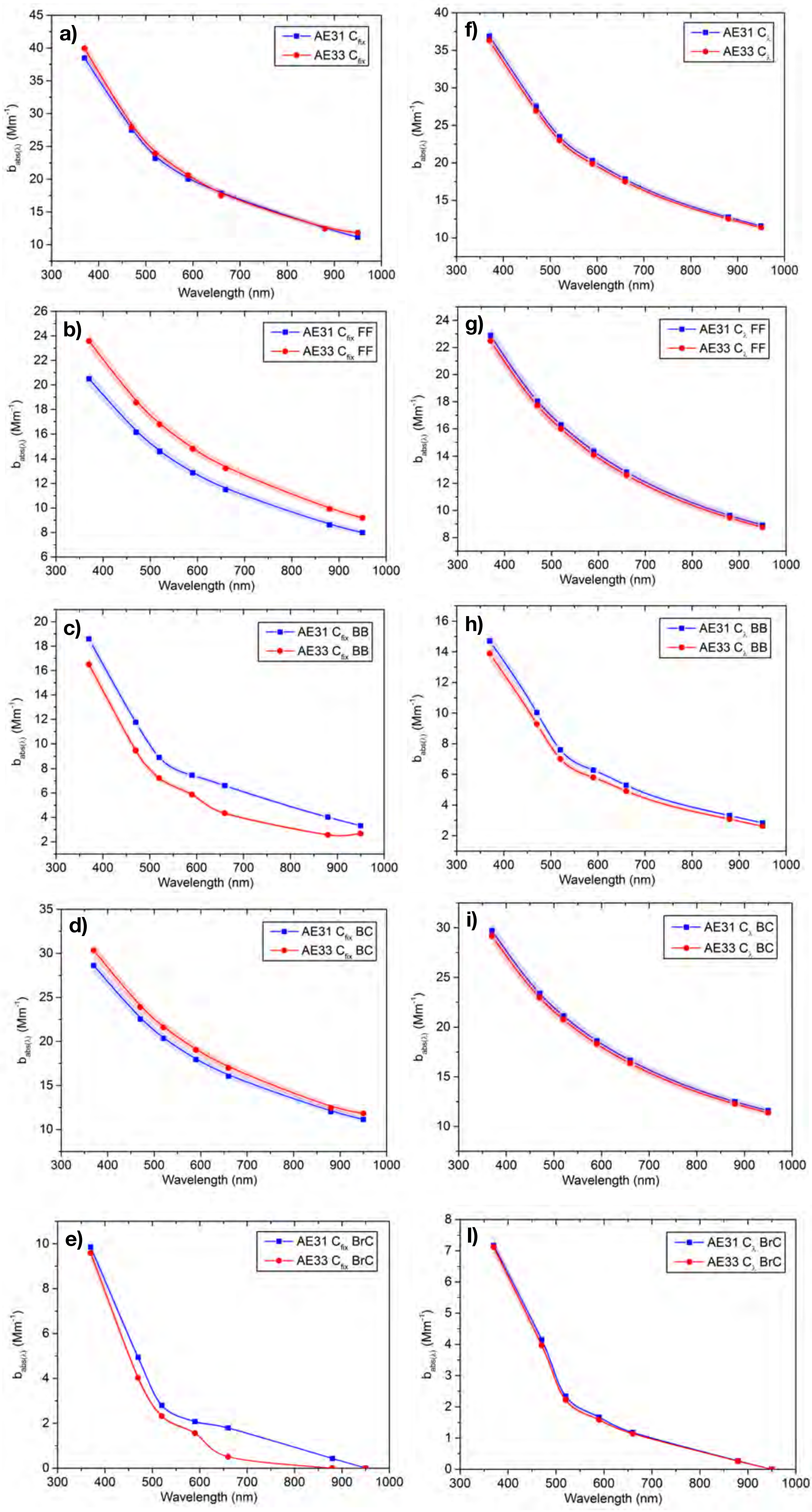
a)
AE31 C fix
AE33 C fix
b)
AE31 C fix FF
AE33 C fix FF
c)
AE31 C fix BB
AE33 C fix BB
d)
AE31 C fix BC
AE33 C fix BC
e)
AE31 C fix BrC
AE33 C fix BrC
f)
AE31 C λ
AE33 C λ
g)
AE31 C λ FF
AE33 C λ FF
h)
AE31 C λ BB
AE33 C λ BB
i)
AE31 C λ BC
AE33 C λ BC
l)
AE31 C λ BrC
AE33 C λ BrC
b abs(λ) (Mm-1)
Wavelength (nm)

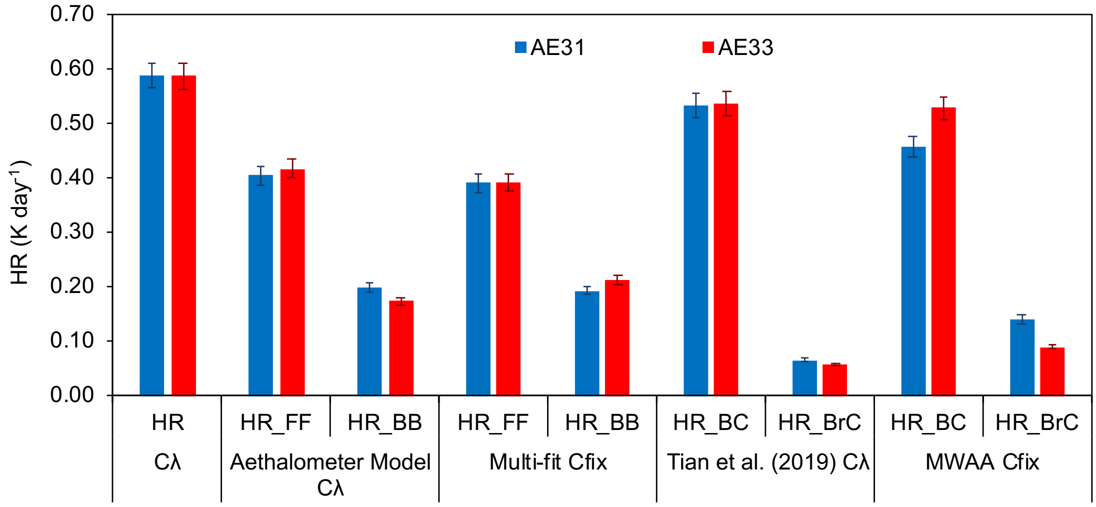
AE31
AE33
HR (K day-1)
0.70
0.60
0.50
0.40
0.30
0.20
0.10
0.00
HR
HR_FF
HR_BB
HR_FF
HR_BB
HR_BC
HR_BrC
HR_BC
HR_BrC
Cλ
Aethalometer Model Cλ
Multi-fit Cfix
Tian et al. (2019) Cλ
MWAA Cfix

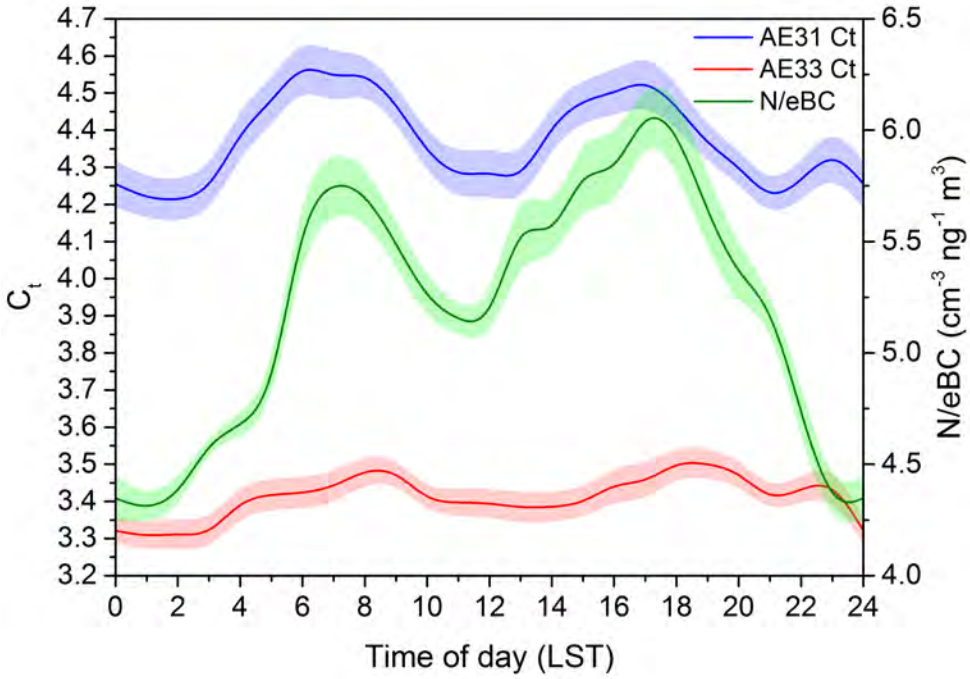
AE31 Ct
AE33 Ct
N/eBC
C_t
N/eBC (cm^{-3} ng^{-1} m^3)
Time of day (LST)
4.7
4.6
4.5
4.4
4.3
4.2
4.1
4.0
3.9
3.8
3.7
3.6
3.5
3.4
3.3
3.2
6.5
6.0
5.5
5.0
4.5
4.0
0 2 4 6 8 10 12 14 16 18 20 22 24

Figure9 Click here to access/download;Figure;Figure_FV9.pdf

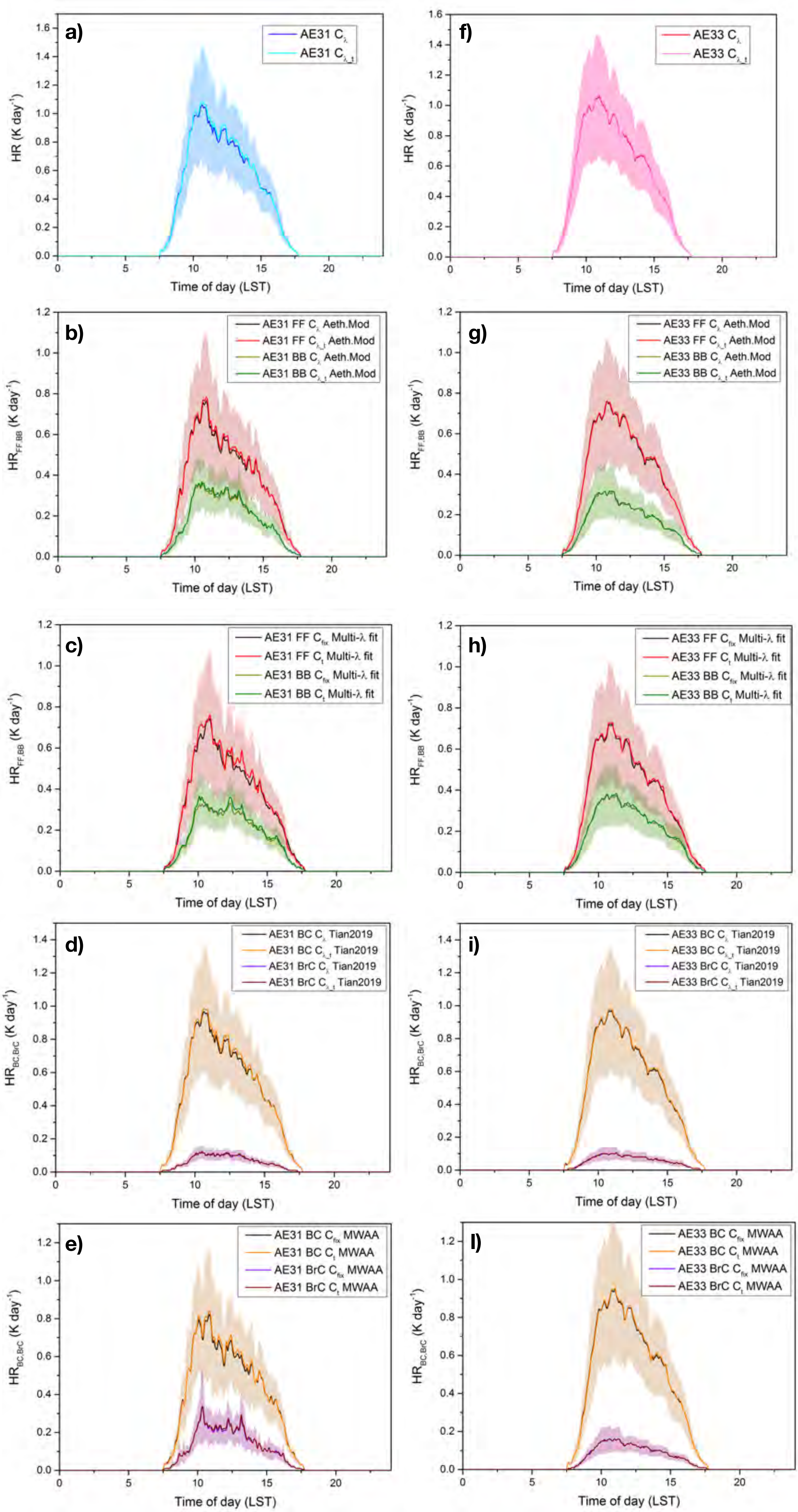

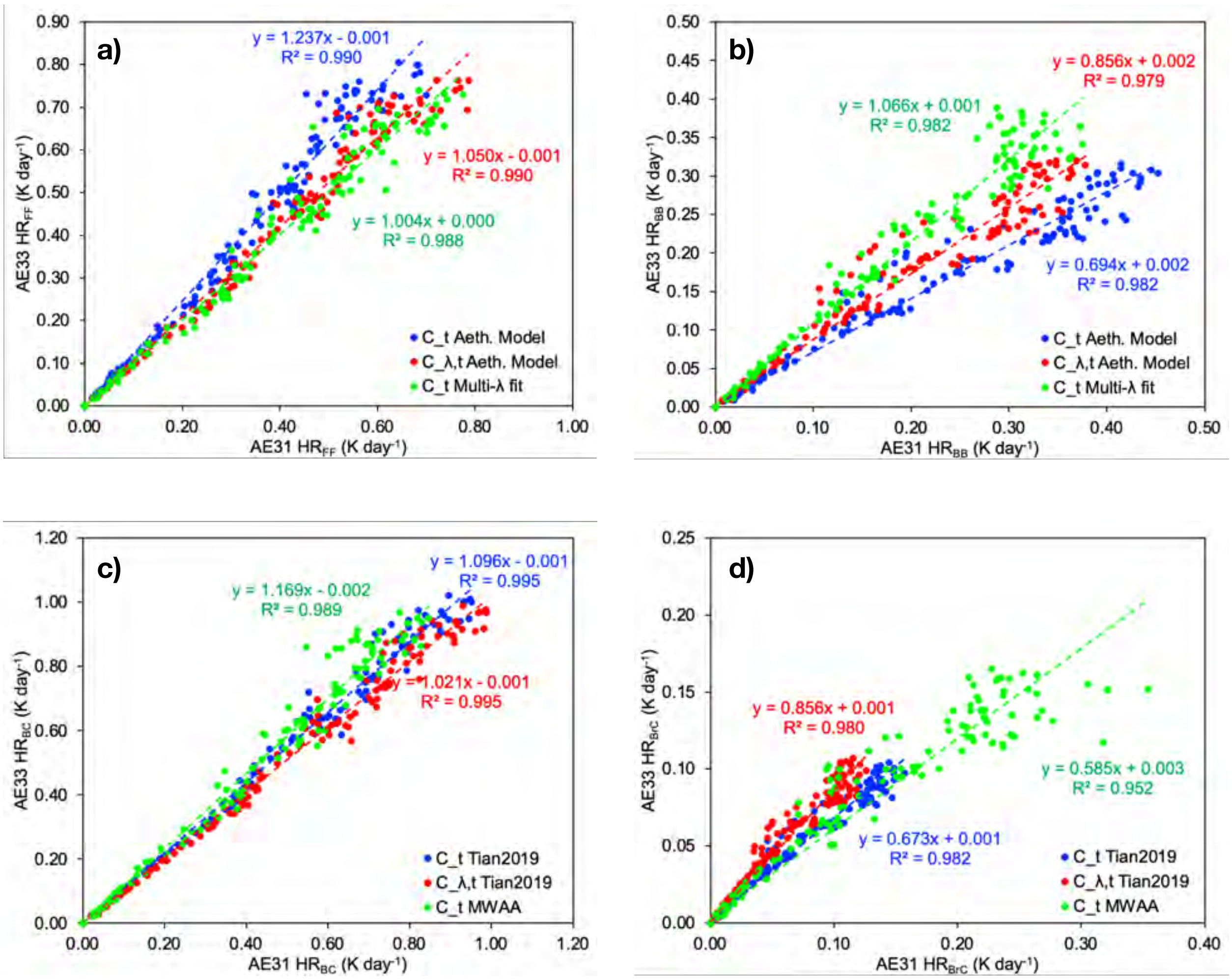
a)
y = 1.237x - 0.001
R² = 0.990
y = 1.050x - 0.001
R² = 0.990
y = 1.004x + 0.000
R² = 0.988
C_t Aeth. Model
C_λ,t Aeth. Model
C_t Multi-λ fit
AE33 HRFF (K day-1)
AE31 HRFF (K day-1)
b)
y = 0.856x + 0.002
R² = 0.979
y = 1.066x + 0.001
R² = 0.982
y = 0.694x + 0.002
R² = 0.982
C_t Aeth. Model
C_λ,t Aeth. Model
C_t Multi-λ fit
AE33 HRBB (K day-1)
AE31 HRBB (K day-1)
c)
y = 1.096x - 0.001
R² = 0.995
y = 1.169x - 0.002
R² = 0.989
y = 1.021x - 0.001
R² = 0.995
C_t Tian2019
C_λ,t Tian2019
C_t MWAA
AE33 HRBC (K day-1)
AE31 HRBC (K day-1)
d)
y = 0.856x + 0.001
R² = 0.980
y = 0.585x + 0.003
R² = 0.952
y = 0.673x + 0.001
R² = 0.982
C_t Tian2019
C_λ,t Tian2019
C_t MWAA
AE33 HRBrC (K day-1)
AE31 HRBrC (K day-1)

Author contribution

Conceptualization: L.F., V.B., E.B., G.V., and R.V. designed and organized the sampling campaign to meet the final goals. L.F. performed the data analysis for heating rate determination and its apportionment in function of the optimized multiple-scattering enhancement parameter and the multi-λ fit approach applied the Aethalometer model. **Data curation:** L.F. and V.B. validated and assembled the final database. **Formal analysis:** L.F., V.B., L.S., S.C., G.M., A.B., N.L., S.V., G.V., D.M and P.P. collaborated to data analysis and reduction. **Methodology:** L.F., V.B., S.C., G.V., R.V. realized the sampling campaign. A.G., M.R., G.M. gave support for Aethalometers set-up. F.S., S.V. performed PP_UniMI measurements. S.C. performed spectroradiometer measurements. **Software:** L.F. developed the software for the heating rate determination and apportionment in function of LAA sources and species. **Supervision:** E.B. and L.F. supervised all the scientific activity. **Writing – original draft:** L.F. and L.S. wrote the original draft. **Writing – review & editing:** all co-authors commented and contributed to the final version of the paper.

Declaration of interests

☒ The authors declare that they have no known competing financial interests or personal relationships that could have appeared to influence the work reported in this paper.

☐The authors declare the following financial interests/personal relationships which may be considered as potential competing interests: